Supplemental material to this article can be found at:
http://jpet.aspetjournals.org/content/suppl/2022/10/30/jpet.122.001116.DC1

1521-0103/384/1/173–186$35.00
THE JOURNAL OF PHARMACOLOGY AND EXPERIMENTAL THERAPEUTICS
dx.doi.org/10.1124/jpet.122.001116
J Pharmacol Exp Ther 384:173–186, January 2023

Copyright © 2022 by The Author(s)
This is an open access article distributed under the CC BY-NC Attribution 4.0 International license.

Identification and Characterization of ACP-5862, the Major Circulating Active Metabolite of Acalabrutinib: Both Are Potent and Selective Covalent Bruton Tyrosine Kinase Inhibitors [S]

Terry Podoll,[1] Paul G. Pearson,[1] Allard Kaptein,[1] Jerry Evarts, Gerjan de Bruin, Maaike Emmelot-van Hoek, Anouk de Jong, Bart van Lith, Hao Sun, Stephen Byard, Adrian Fretland, Niels Hoogenboom, Tjeerd Barf, and J. Greg Slatter

Acerta Pharma (a member of the AstraZeneca group), South San Francisco, California (T.P., J.E., A.F., J.G.S.); Acerta Pharma (a member of the AstraZeneca group) Oss, The Netherlands (G.d.B., M.E.-v.H., A.d.J., B.v.L., N.H.); Pearson Pharma Partners, Westlake Village, California (P.G.P.); Covance Laboratories, Madison, Wisconsin (H.S.); Arcinova, Alnwick, United Kingdom (S.B.); and Covalution Holding B.V., Ravenstein, The Netherlands (A.K., T.B.)

Received January 19, 2022; accepted October 17, 2022

ABSTRACT

Acalabrutinib is a covalent Bruton tyrosine kinase (BTK) inhibitor approved for relapsed/refractory mantle cell lymphoma and chronic lymphocytic leukemia/small lymphocytic lymphoma. A major metabolite of acalabrutinib (M27, ACP-5862) was observed in human plasma circulation. Subsequently, the metabolite was purified from an in vitro biosynthetic reaction and shown by nuclear magnetic resonance spectroscopy to be a pyrrolidine ring–opened ketone/amide. Synthesis confirmed its structure, and covalent inhibition of wild-type BTK was observed in a biochemical kinase assay. A twofold lower potency than acalabrutinib was observed but with similar high kinase selectivity. Like acalabrutinib, ACP-5862 was the most selective toward BTK relative to ibrutinib and zanubrutinib. Because of the potency, ACP-5862 covalent binding properties, and potential contribution to clinical efficacy of acalabrutinib, factors influencing acalabrutinib clearance and ACP-5862 formation and clearance were assessed. rCYP (recombinant cytochrome P450) reaction phenotyping indicated that CYP3A4 was responsible for ACP-5862 formation and metabolism. ACP-5862 formation K_m (Michaelis constant) and V_{max} were 2.78 μM and 4.13 pmol/pmol CYP3A/min, respectively. ACP-5862 intrinsic clearance was 23.6 μL/min per mg. Acalabrutinib weakly inhibited CYP2C8, CYP2C9, and CYP3A4, and ACP-5862 weakly inhibited CYP2C9 and CYP2C19; other cytochrome P450s, UGTs (uridine 5′-diphospho-glucuronosyltransferases), and aldehyde oxidase were not inhibited. Neither parent nor ACP-5862 strongly induced CYP1A2, CYP2B6, or CYP3A4 mRNA. Acalabrutinib and ACP-5862 were substrates of multidrug resistance protein 1 and breast cancer resistance protein but not OATP1B1 or OATP1B3. Our work indicates that ACP-5862 may contribute to clinical efficacy in acalabrutinib-treated patients and illustrates how proactive metabolite characterization allows timely assessment of drug-drug interactions and potential contributions of metabolites to pharmacological activity.

SIGNIFICANCE STATEMENT

This work characterized the major metabolite of acalabrutinib, ACP-5862. Its contribution to the pharmacological activity of acalabrutinib was assessed based on covalent Bruton tyrosine kinase binding kinetics, kinase selectivity, and potency in cellular assays. The metabolic clearance and in vitro drug-drug interaction potential were also evaluated for both acalabrutinib and ACP-5862. The current data suggest that ACP-5862 may contribute to the clinical efficacy observed in acalabrutinib-treated patients and demonstrates the value of proactive metabolite identification and pharmacological characterization.

Introduction

Acalabrutinib (Calquence; https://den8dhaj6zs0e.cloudfront.net/50fd68b9-106b-4550-b5d0-12b045f8b184/e2a005a7-65a0-4388-a671-dc887815a938/e2a005a7-65a0-4388-a671-dc887815a938_viewable_rendition__v.pdf) is a potent, highly selective, next-gene-ration, targeted covalent inhibitor of Bruton tyrosine kinase (BTK) approved in adults with previously treated mantle cell lymphoma and in patients with chronic lymphocytic leukemia or small lymphocytic lymphoma. Covalent inhibition of BTK is a clinically validated mechanism for the treatment of B-cell malignancies (Ponader and Burger, 2014). Other approved covalent kinase inhibitors such as ibrutinib (BTK), osimertinib [epidermal growth factor receptor (EGFR)], and neratinib [EGFR, human epidermal growth factor receptor (HER)-2, and HER4], and afatinib (EGFR, HER2, and HER4) contain acrylamide-based electrophiles

---

This study was supported by Acerta Pharma, a member of the AstraZeneca Group.

T.P. and J.E. were employed by Acerta Pharma at the time of the study, hold Acerta Pharma patents, and hold AstraZeneca stock. J.G.S. was employed by Acerta Pharma at the time of the study and holds AstraZeneca stock. A.F. was employed by Acerta Pharma at the time of the study. G.d.B., A.d.J., and N.H. are employees of Acerta Pharma B.V. M.E.-v.H. and B.v.L. are employees and stockholders of Acerta Pharma B.V. P.G.P. is an employee of Pearson Pharma Partners, which was hired by Acerta Pharma during the time of the study to serve in a consultancy capacity, and holds AstraZeneca stock. A.K. and T.B. are employees of Covalution Biosciences B.V., Ravenstein, The Netherlands, which was hired by Acerta Pharma during the time of the study to serve in a consultancy capacity, and hold Acerta Pharma B.V. stock. H.S. was an employee of Covance Laboratories, which was hired by Acerta Pharma during the time of the study to serve in a consultancy capacity. S.B. is an employee of Arcinova, which was hired by Acerta Pharma during the time of the study to serve in a consultancy capacity.

[1] T.P., P.G.P., and A.K. contributed equally to this work.

dx.doi.org/10.1124/jpet.122.001116.

[S] This article has supplemental material available at jpet.aspetjournals.org.

that generally have higher reactivity relative to the butynamide in acalabrutinib (Podoll et al., 2019; https://nerlynxhcp.com/pdf/full-prescribing-information.pdf; https://content.boehringer-ingelheim.com/DAM/07c11f94-358a-439d-b0c8-af1e011f04c4/gilotrif-us-pi.pdf; https://www.imbruvica.com/files/prescribing-information.pdf; https://den8dhaj6zs0e.cloudfront.net/50fd68b9-106b-4550-b5d0-12b045f8b184/52503580-1192-44f7-a05e-5743159ed19b/52503580-1192-44f7-a05e-5743159ed19b_viewable_rendition__v.pdf). The electrophile is the moiety that binds the selected cysteine thiol nucleophiles in the ATP binding pocket of a protein kinase to provide the covalent bond (Barf et al., 2017; Podoll et al., 2019). Covalent inhibitors with highly reactive acrylamide-based electrophiles are very effective in inhibiting their respective protein kinase target but may lack selectivity, which could result in off-target binding to kinases and nonkinase proteins (Chandrasekaran et al., 2010; Stopfer et al., 2012; Scheers et al., 2015; Dickinson et al., 2016). Compared with the other BTK inhibitors approved for clinical use (ibrutinib, zanubrutinib), acalabrutinib has demonstrated greater selectivity for BTK in vitro and reduced inhibition of signaling through EGFR, interleukin-2–inducible T-cell kinase (ITK), Tec protein tyrosine kinase (TEC), and Src family kinases (Byrd et al., 2016; Barf et al., 2017; Kaptein et al., 2018). Lower off-target binding to protein kinases and biologic nucleophiles in general may yield an improved safety profile for acalabrutinib compared with other BTK inhibitors (Singh et al., 2011; Pal Singh et al., 2018).

The 2-butynamide electrophile in acalabrutinib is positioned in proximity to the Cys481 nucleophile at the rim of the ATP binding pocket (Barf et al., 2017). Unlike drugs that interact reversibly with their targets and generally require sustained plasma levels to achieve target coverage over the dose interval, potent covalent inhibitors such as acalabrutinib can drive high target occupancy after a relatively brief systemic exposure (Baillie, 2016; Lonsdale and Ward, 2018). This can result in prolonged pharmacodynamic effects, with the duration of effect related to the time required for target resynthesis (Singh et al., 2011; Barf and Kaptein, 2012). Acalabrutinib has rapid absorption and a short plasma half-life, key pharmacokinetic (PK) characteristics of safe and effective covalent inhibitors (Byrd et al., 2016; Barf et al., 2017). Because pharmacologically active metabolites may contribute to the overall efficacy of any treatment, they must be considered when evaluating overall efficacy and/or safety, especially when formed at pharmacologically relevant concentrations.

Early studies characterized several metabolites of acalabrutinib that are related to glutathione (GSH) conjugation of the 2-butynamide electrophile and were later confirmed to be minor metabolites (Podoll et al., 2019). The major metabolite of acalabrutinib was first identified by mass-defect filter high-performance liquid chromatography (HPLC)–high resolution mass spectroscopy in clinical plasma samples as an abundant, +16 Da, oxidized metabolite (M27) that eluted after acalabrutinib; however, it was not quantified, and fragmentation did not reveal the regiochemistry of oxidation. Subsequently, results from a [^{14}C]microtracer human absorption, distribution, metabolism, and excretion and bioavailability study demonstrated 25% absolute bioavailability of acalabrutinib, rapid radioactivity excretion mainly in feces, and near-complete radiolabel recovery (Podoll et al., 2019). One major, late-eluting oxidized metabolite was observed that matched the retention time of M27 (ACP-5862) (Fig. 1) (Podoll et al., 2019). ACP-5862 comprised 35% of total drug-related material in plasma, representing fourfold higher systemic exposure than the parent acalabrutinib, based on time-proportional pooling in six healthy volunteers.

The objective of this study was to characterize acalabrutinib's major metabolite and assess its potential contribution to pharmacological activity during acalabrutinib therapy. Herein, we report the covalent BTK binding kinetics, kinase selectivity, and potency in cellular assays for acalabrutinib and ACP-5862. Ibrutinib and zanubrutinib were included to allow direct comparison of acrylamide versus butynamide electrophile attributes. The potential for drug-drug interactions with acalabrutinib and ACP-5862 was determined to elucidate intrinsic and extrinsic factors that may influence their exposure-response relationships (Baillie et al., 2002; Edlund et al., 2019; Zhou et al., 2019; Edlund et al., 2022a; https://www.fda.gov/regulatory-information/search-fda-guidance-documents/safety-testing-drug-metabolites). Purification and structural elucidation of the M27 in vitro metabolite by NMR spectroscopy enabled subsequent chemical synthesis of ACP-5862 (M27), and the proposed mechanism of its formation is first reported herein.

Materials and Methods

Materials. Radiolabeled acalabrutinib (1,4-[8-amino-3-[(2S)-1-but-2-ynoylpyrrolidin-2-yl]imidazo[1,5-α]pyrazin-1-yl]-*N*-(2-pyridyl)-benzamide), labeled at the carboxyl carbon atom of the 2-pyridylbenzamide portion of the molecule (Fig. 1), was prepared with a [^{14}C]acalabrutinib radioactivity content of 57 mCi/mmol. The radiochemical purity of [^{14}C]acalabrutinib was verified at the beginning and end of the metabolite preparation incubations using an HPLC method. Metabolite reference standard materials were prepared by Kalexsyn (Kalamazoo, MI) or Acerta Pharma, BV (Oss, Netherlands) (https://patentimages.storage.googleapis.com/6a/e5/44/abb83f5c5dcc87/US20190345164A1.pdf). 1-Chloro-2,4-dinitrobenzene was purchased from Sigma-Aldrich Chemical Co. (St. Louis, MO). Pooled human liver microsomes (HLMs) were obtained from BioreclamationIVT (Baltimore, MD) and were stored at approximately −70°C. Cryopreserved human hepatocytes were supplied by XenoTech, LLC (Kansas City, KS) for assessment of the induction of cytochrome P450 (P450) enzymes by acalabrutinib and ACP-5862. Bactosomes containing individually expressed P450 enzymes or control expression plasmid without P450 in *Escherichia coli* membranes were obtained from Cypex, Ltd. (Dundee, UK). Human embryonic kidney 293 (HEK293) cells

---

ABBREVIATIONS: ACN, acetonitrile; AUC, area under the curve; BCRP, breast cancer resistance protein; BLK, B-lymphocyte kinase; BMX, BMX nonreceptor tyrosine kinase; BTK, Bruton tyrosine kinase; BTK-WT, wild-type BTK; Cl_{int}, intrinsic clearance; EGFR, epidermal growth factor receptor; ERBB2, erythroblastosis oncogene B2; ERBB4, erythroblastosis oncogene B4; GSH, glutathione; GST, glutathione S-transferase; HEK293, human embryonic kidney 293; HER, human epidermal growth factor receptor; HLM, human liver microsome; HPLC, high-performance liquid chromatography; IMAP, immobilized metal ion affinity-based fluorescence polarization; ITK, interleukin-2–inducible T-cell kinase; JAK3, Janus-associated kinase 3; K_I, inhibitory constant; k_{inact}, inactivation rate constant; k_{inact}/K_I, second-order rate constants; K_m, Michaelis constant; LC-MS/MS, liquid chromatography with tandem mass spectrometry; MDCKII, Madin-Darby canine kidney; MeOH, methanol; P450, cytochrome P450; PBMC, peripheral blood mononuclear cell; P-gp, P-glycoprotein; PK, pharmacokinetic; rCYP, recombinant cytochrome P450; TEC, Tec protein tyrosine kinase; TXK, TXK tyrosine kinase/protein tyrosine kinase 4; UGT, uridine 5′-diphospho-glucuronosyltransferase; WB, whole blood.

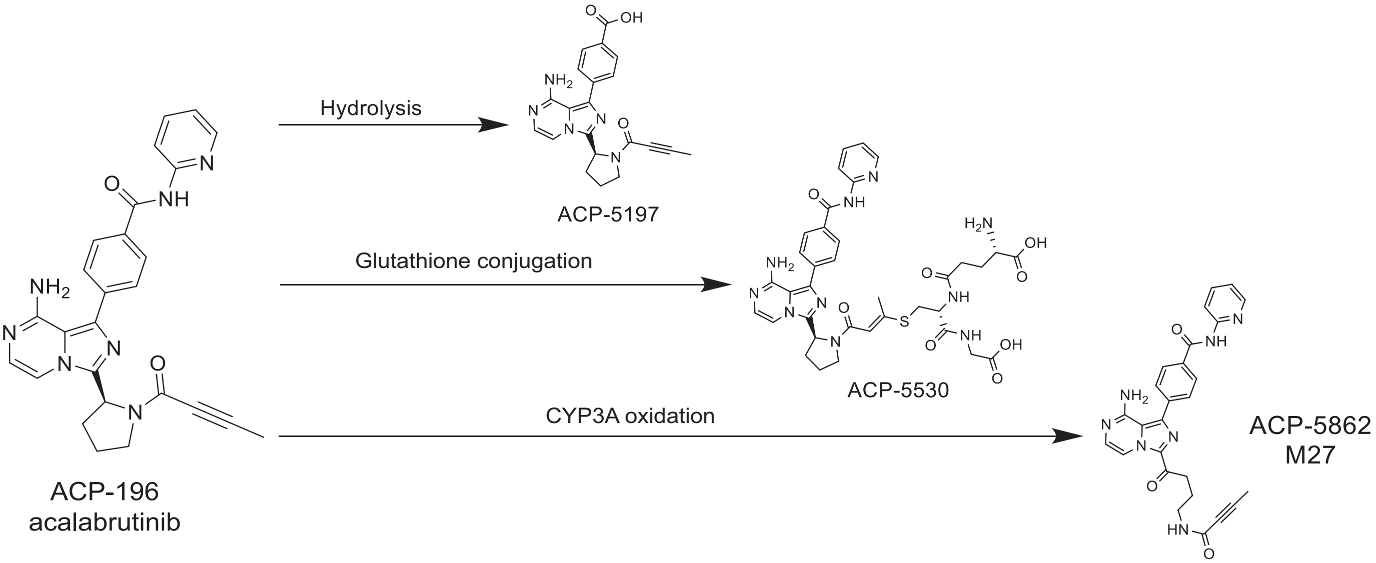

Fig. 1. Metabolism of acalabrutinib: primary metabolic routes.

and Caco-2 cells were obtained from American Type Culture Collection (Manassas, VA). The HEK293 cells were transfected with the individual transporter genes by Sekisui Medical Co. Ltd. (Tokyo, Japan). Madin-Darby canine kidney (MDCKII) cells overexpressing human P-glycoprotein (P-gp; multidrug resistance protein 1) and breast cancer resistance protein (BCRP) were obtained from the Netherlands Cancer Institute (Amsterdam). All other reagents and chemicals were obtained from standard commercial sources. In addition, plasma samples collected from patients receiving repeated oral doses of acalabrutinib in a phase 1/2 study (#NCT02029443) were used in the analysis of the M25 and M27 metabolites; that study was conducted according to the principles of the Declaration of Helsinki and the International Conference on Harmonization Good Clinical Practice, and informed written consent was obtained from all patients.

Biochemical Kinase Assays. BTK and ITK (Millipore, Dundee, UK) enzyme activities were measured as described previously using the immobilized metal ion affinity-based fluorescence polarization (IMAP) assay(Barf et al., 2017). IC_{50} measurements over time were obtained using LanthaScreen (Thermo Fisher Scientific, Carlsbad, CA) for wild-type BTK (BTK-WT) and C481S (Barf et al., 2017) under conditions in which the reaction was linear with time in the absence or presence of inhibitor; from these time-dependent experiments, inactivation rate constant (k_{inact}) and inhibitory constant (K_I) values were obtained using the method of Krippendorff et al. (2009) as described previously (Barf et al., 2017).

The inhibition kinase activity for TEC was measured using the LanthaScreen assay (Thermo Fisher Scientific), and the inhibition of BMX nonreceptor tyrosine kinase (BMX), TXK tyrosine kinase/protein tyrosine kinase 4 (TXK), EGFR, erythroblastosis oncogene B2 (ERBB2), erythroblastosis oncogene B4 (ERBB4), B-lymphocyte kinase (BLK), and Janus-associated kinase 3 (JAK3) was measured using the Z′-LYTE assay (Thermo Fisher Scientific) as described previously (Barf et al., 2017).

The ATP concentrations in all IMAP, LanthaScreen, and Z′-LYTE assays were set at the Michaelis constant (K_m) ATP for each kinase to enable comparative selectivity profiles between kinase inhibitors. Similarly, the overall kinase selectivity was assessed using kinome profiling at a single inhibitor dose (1 μM) using KINOMEscan (Eurofins DiscoverX) (Fabian et al., 2005; Herman et al., 2017) because it does not require ATP or phosphorylation substrate, enabling direct comparison of the relative binding affinities of the kinase inhibitors.

B-Cell Inhibition of BCR-Induced CD69 Surface Expression in Human Peripheral Blood Mononuclear Cells and Human Whole Blood. BTK inhibition in whole-cell assays was conducted as described previously (Barf et al., 2017). Briefly, cryopreserved peripheral blood mononuclear cells (PBMCs) were suspended in RPMI 1640 plus 10% FBS (2×10^5 cells per well) and incubated with acalabrutinib and ACP-5862 (0.316 to 10,000 nM) for 2 hours at 37°C, 5% CO_2. Goat anti-human IgM F(ab′)2 (Southern Biotech, Birmingham, AL) was then added, and cells were incubated for an additional 18 hours. For the whole-blood (WB) assay, 45 μl blood was diluted 1:1 in RPMI 1640 plus 1% FBS and incubated with test compound (as described above). WB was stimulated with 10 μg/ml mouse antihuman anti-IgD (BD Biosciences) and incubated for 18 hours. PBMCs or WB were stained with CD69-fluorescein isothiocyanate, CD19-BV421, and CD3-BV510 antibodies (BD Biosciences, San Diego, CA), with 7-aminoactinomycin D as a viability measure. To lyse red blood cells, WB was treated with fluorescence-activated cell sorter lysing solution (BD Biosciences), washed, pelleted, and resuspended in 200 μl per well PBS plus 0.5% bovine serum albumin before flow cytometry. For both the PBMC and WB assays, the median fluorescence intensity values for CD69 were obtained from the $CD19^+$ $CD3^-$ B-lymphocyte gate using FCS Express analysis software (De Novo Software, Glendale, CA). EC_{50} values were determined based on curve fitting of experimental results using Dotmatics.

Metabolism of Acalabrutinib and ACP-5862 in Vitro: P450 Enzyme Identification. The metabolism of acalabrutinib and ACP-5862 (1 μM) were investigated in the presence and absence of P450 isoform-selective chemical inhibitors under conditions in which the reaction was linear with time. HLMs (0.1 and 0.5 mg/ml protein for acalabrutinib and ACP-5862, respectively) were incubated at 37°C with 10 μM furafylline (CYP1A2), 30 μM phencyclidine (CYP2B6), 100 μM gemfibrozil glucuronide (CYP2C8), 20 μM tienilic acid (CYP2C9), 10 μM esomeprazole (CYP2C19), 10 μM quinidine (CYP2D6), 5 μM paroxetine [CYP2D6 (ACP-5862 only)], 10 μM diethyldithiocarbamate (CYP2E1), 50 μM troleandomycin (CYP3A4), or 1 μM ketoconazole [CYP3A4/5 (acalabrutinib only)]. Reactions utilizing metabolism-dependent inhibitors (furafylline, phencyclidine, gemfibrozil glucuronide, tienilic acid, esomeprazole, paroxetine, diethyldithiocarbamate, or troleandomycin) were incubated with the HLMs and an NADPH-generating system for 30 minutes at 37°C prior to initiating the reaction by the addition of acalabrutinib or ACP-5862. Reactions utilizing direct inhibitors (quinidine or ketoconazole) were initiated with the addition of an NADPH-generating system consisting of NADP (1 mM, pH 7.4), glucose-6-phosphate (5 mM, pH 7.4), and glucose-6-phosphate dehydrogenase (1 U/ml). All incubations also contained

50 mM potassium phosphate buffer (pH 7.4), $MgCl_2$ (3 mM), and EDTA (1 mM) and were terminated after 60 and 45 minutes for acalabrutinib and ACP-5862, respectively, by the addition of an equal volume of acetonitrile (ACN) containing their respective deuterium-labeled internal standards. The samples were centrifuged (e.g., 920*g* for 10 minutes at 10°C). The supernatant fractions were analyzed by liquid chromatography with tandem mass spectrometry (LC-MS/MS) to quantify the amount of acalabrutinib and ACP-5862 remaining based on a calibration curve.

Membranes isolated from *E. coli* expressing individual cytochrome P450 enzymes rCYP1A2, rCYP2B6, rCYP2C8, rCYP2C9, rCYP2C19, rCYP2D6, and rCYP3A4 were incubated with acalabrutinib (1 and 10 μM) and ACP-5862 (0.1 and 1.0 μM) at 10 and 2.5 pmol P450 per incubation, respectively. The content and conduct of the incubations and subsequent sample preparation steps were similar to those described above. Consumption of acalabrutinib and ACP-5862 in the presence of individual P450s was compared with that observed in membranes from vector control *E. coli* membranes.

ACP-5862 initial-rate formation kinetics were measured in HLM (0.1 mg/ml) during a 6-minute reaction time and in rCYP3A4 (12.5 pmol/ml) during a 4-minute reaction time over an acalabrutinib concentration range of 0.7–70 μM and 1.5–150 μM, respectively. ACP-5862 (0.1 μM) in vitro intrinsic clearance (Cl_{int}) was measured in HLM (0.5 mg/ml) by monitoring its disappearance after 5, 15, 30, and 45 minutes in the presence of NADPH (1-mM generating system as described above). The Cl_{int} was determined using the following equation:

$$Cl_{int} = \left(0.693/t_{1/2}\right) \times 2000\ \mu l/\mathrm{mg\ protein} \qquad (1)$$

Metabolism of Acalabrutinib in Vitro: Glutathione S-Transferase Enzyme Identification. Metabolism of acalabrutinib (1.0, 10, and 100 μM) was investigated in human liver cytosol (up to 2.0 mg/ml protein) incubated up to 120 minutes at 37°C with and without supplementation with reduced GSH (0.6 mM). Additionally, metabolism of acalabrutinib (100 μM) was investigated across a panel of individually expressed recombinant human glutathione s-transferase (GST) enzymes (rGSTA1, A2, M1, M2, P1, and T1 at 0.1 and 0.5 mg protein per ml). Incubation at 37°C was initiated by the addition of acalabrutinib and terminated at 0 and 120 minutes by the addition of an equal volume of acetonitrile. In all experiments, acalabrutinib was analyzed by LC-MS/MS to quantify the amount of acalabrutinib remaining based on a calibration curve. Additionally, the formation of GSH, cysteine-glycine, and cysteine conjugates of acalabrutinib (M5, ACP-5530; M7, ACP-5531; and M10, ACP-5461) (Podoll et al., 2019) was monitored by LC-MS/MS using the ratio of metabolite to internal standard. Incubations of 1-chloro-2,4-dinitrobenzene with human liver cytosol and each recombinant enzyme were analyzed using colorimetric analysis to quantify glutathione conjugate formation and to ensure that the test systems were metabolically competent.

P450 Inhibition by Acalabrutinib and ACP-5862. Coincubation of acalabrutinib or ACP-5862 with P450 enzyme–selective substrates was performed to determine their potential to cause drug-drug interactions in a manner similar to that previously described (Paris et al., 2009). The formation of acetaminophen, 8-hydroxyefavirenz, *N*-desethylamodiaquine, 4′-hydroxydiclofenac, 4′-hydroxymephenytoin, dextrorphan, 6*β*-hydroxytestosterone, and 1′-hydroxymidazolam were individually quantified as markers for CYP1A2, CYP2B6, CYP2C9, CYP2C19, CYP2D6, CYP3A4/5, and CYP3A4/5 again, respectively, following incubations with pooled, mixed-gender HLMs (≤0.1 mg protein per ml). Acalabrutinib or ACP-5862 were coincubated with the marker substrates in duplicate at concentrations up to 100 or 20 μM, respectively. Metabolism- and time-dependent inhibition of each P450 by acalabrutinib and ACP-5862 up to their respective concentrations stated above was assessed by conducting 30-minute preincubations in the presence and absence of the NADPH-generating system. Reversibility was assessed, and samples were analyzed by LC-MS/MS as described previously (Watanabe et al., 2007; Paris et al., 2009). The respective metabolite formation from each probe substrate was compared with that observed for the solvent control incubations. To determine the k_{inact} and K_I values for the inactivation of P450s, primary incubations of acalabrutinib or ACP-5862 with HLMs at approximately 0.1 mg/mL and an NADPH-generating system were conducted for 0, 3, 6, 9, 15, and 30 minutes. The mixtures were then diluted 10-fold into secondary incubation tubes containing the marker substrate [near saturable rate (V_{max}) concentrations] and an NADPH-generating system to arrest any inactivation by the inhibitor and measure residual activities for 5 minutes. The rates of enzyme inactivation at each inhibitor concentration were determined to calculate the k_{inact} and K_I values as described previously (Kitz and Wilson, 1962; Jones et al., 1999).

UGT1A1 and UGT2B7 Inhibition by Acalabrutinib and ACP-5862. Coincubation of acalabrutinib or ACP-5862 with UGT enzyme–selective substrates was also performed. The formation of estradiol 3-glucuronide and zidovudine 5′-glucuronide was individually quantified as markers for UGT1A1 and UGT2B7, respectively, following incubations with pooled, mixed-gender HLMs (0.2 mg protein per ml). Acalabrutinib or ACP-5862 was coincubated with the marker substrates in duplicate over the concentration range from 0.003 to 3 μM.

P450 Induction by Acalabrutinib and ACP-5862. Acalabrutinib and ACP-5862 were tested individually for their capacity to induce the expression of P450 enzymes in primary cultures of freshly isolated human hepatocytes from three individual donors (48-year-old female Caucasian, 57-year-old female Caucasian, and 56-year-old male Caucasian for acalabrutinib; 39-year-old female Caucasian, 57-year-old female Caucasian, and 61-year-old male Caucasian for ACP-5862), similar to methods previously described (Robertson et al., 2000; Paris et al., 2009). The hepatocytes were treated once daily for 3 consecutive days with acalabrutinib and ACP-5862 (up to 50 μM). Cultures were also treated with flumazenil (25 μM, negative control) or 1 of 3 known human P450 enzyme inducers, omeprazole (50 μM), phenobarbital (750 μM), and rifampicin (20 μM). Induction was measured by changes in P450 mRNA expression assessed by quantitative reverse-transcription polymerase chain reaction assays selective for CYP1A2, CYP2B6, and CYP3A4.

In Vitro Efflux and Uptake Transporter Inhibition. Coincubation of acalabrutinib or ACP-5862 with various substrates of human efflux and uptake transporters was performed to evaluate inhibition of transporters in cell lines (Kazmi et al., 2018). The bidirectional permeability of specific probe substrates for P-gp (digoxin, 10 μM in Caco-2 cells) and BCRP (prazosin, 1 μM in MDCKII cells) was measured in the presence of acalabrutinib (up to 400 μM) or ACP-5862 (up to 20 and 50 μM for P-gp and BCRP, respectively) by adding them to both apical and basolateral sides for 120 minutes before stopping with the addition of methanol:water (50:50, v:v) and analysis by LC-MS/MS. Under the condition of the assay, the recovery of the probe substrate (digoxin) ranged from 91.2% to 112%, and valspodar and verapamil (positive controls) inhibited the transport of digoxin in an expected manner.

During uptake assays, HEK293 cells were preincubated with acalabrutinib or ACP-5862 [up to 20 μM for OATP1B and OATP1B3 (0.05 μM [^{3}H]estradiol 17*β*-glucuronide as substrate), OAT1 (1 μM para-aminohippurate as substrate), OAT3 (50 nM estrone sulfate as substrate), and OCT2 (10 μM metformin as substrate); up to 3 μM for MATE1 and MATE2-K (10 μM metformin as substrate)] for 15 minutes, followed by a 1- to 5-minute incubation with both radiolabeled probe substrate and acalabrutinib or ACP-5862, and then stopped by aspiration and washed as previously described (Kazmi et al., 2018). Incubations were repeated for OATP1B1- and OAT1-expressing cells for ACP-5862 (up to 50 μM). Cells were extracted (0.1N NaOH), and scintillation counting was conducted (Microbeta2, Perkin Elmer, Waltham, MA) to quantify uptake.

In Vitro Efflux and Uptake Transporter Substrate Determination. The bidirectional permeability of acalabrutinib [1, 3 (BCRP only), 10, and 30 (P-gp only) μM] and ACP-5862 (2, 10, and 50 μM) across MDCKII–P-gp cells (acalabrutinib only), Caco-2 cells, or MDCKII-BCRP cells was measured to evaluate each as substrates of P-gp or BCRP as described previously (Brouwer et al., 2013). After the cells were confluent, transport was measured from apical to basolateral and basolateral to apical with samples being collected from the receiver compartment after 15 (acalabrutinib only), 30 (acalabrutinib only), and 120 minutes of incubation, mixed with their respective deuterium-labeled internal standards, and quantified for substrate content by LC-MS/MS.

The cellular uptake of acalabrutinib or ACP-5862 was assessed in HEK293 cells transfected with OATP1B1, OATP1B3, or vector control. Acalabrutinib was tested at 1, 3, and 10 μM and ACP-5862 at 2, 10, and 50 μM, with both at 1- to 10-minute incubation times. The maximum influx uptake ratio (the influx rate of the test compound in transfected cells over that in nontransfected cells) was measured by quantifying the accumulation of each test substrate by LC-MS/MS. The cellular uptake of acalabrutinib was similarly assessed in HEK293 cells transfected with OAT1, OAT3, and OCT2 or vector control. Acalabrutinib was tested at 1, 10, and 30 μM and at 1-, 3-, and 10-minute incubation times. ACP-5862 was not tested as a substrate for renal influx transporters.

Metabolite M27 (ACP-5862) Preparative Scale Biosynthesis. [^{14}C]Acalabrutinib (10 μM, 4280 μCi/mmol) was incubated with pooled, mixed-sex HLMs (2 mg protein per ml) in 100 mM potassium phosphate buffer (pH 7.4) with nicotinamide adenine dinucleotide phosphate, reduced form (NADPH, 2 mM), at 37°C for 30 minutes in a shaking water bath (10 replicates at 20 ml each). Incubations were terminated by the addition of an equal volume of ACN. The organic phase was separated from the proteins by centrifugation. A portion (800 μl) of each sample was evaporated to dryness under nitrogen, reconstituted in 300 μl of water:methanol (MeOH; 9:1, v:v), and centrifuged at 1430*g* for 10 minutes. The remaining supernatants were concentrated to approximately 10 ml each under a vacuum and combined. Samples were stored at −70°C until analysis by liquid chromatography–high-resolution mass spectrometry (LTQ Orbitrap XL with electrospray ionization, Thermo Fisher, Wilmington, DE) with in-line radiochromatographic detection. Radioactivity recoveries were determined throughout the sample processing procedures. Cytochrome P450 activities of the HLMs were assessed with midazolam (1 μM).

Samples were loaded onto conditioned solid-phase extraction columns, washed with water, and eluted with 10 ml of MeOH. The MeOH eluents were combined, evaporated to dryness under nitrogen, and reconstituted in 1 ml of 9:1 (v:v) water:MeOH. The samples were then extracted twice with 3 ml of ACN, sonicated, vortex mixed, and centrifuged (1430*g* for 10 minutes). The combined supernatants were evaporated to dryness under nitrogen and reconstituted in 500 μl of 9:1 (v:v) water:MeOH. The sample was sonicated, vortex mixed, and centrifuged. This supernatant was removed and set aside for HPLC analysis. The remaining pellet was further reconstituted and extracted as described previously to increase the recovery. The reconstituted pellet supernatants were evaporated to dryness under nitrogen, reconstituted in 400 μl of 1:1 (v:v) water:MeOH, and centrifuged. Details for purification of combined fractions of metabolites M25 and M27 are provided in the Supplemental Methods. ACP-5862 NMR sample preparation and experiments are also described in the Supplemental Methods.

Statistical Analysis. Descriptive statistics (mean and standard deviation) were calculated and reported where appropriate.

Results

Preclinical Pharmacological Profiling. BTK enzymatic activity was measured using an IMAP assay. Acalabrutinib and ACP-5862 had comparable biochemical potencies, with an IC_{50} value of approximately 5 nM for both parent and major metabolite (Table 1). Additionally, BTK kinase binding assays were performed using BTK-WT and a mutant form of BTK with Cys481Ser to confirm the covalent inhibition of BTK by acalabrutinib and ACP-5862 and investigate the binding kinetics for parent and metabolite (Fig. 2). The K_I is comparable for acalabrutinib and ACP-5862 (Table 2), indicating that both parent and metabolite have similar apparent affinity for BTK. The k_{inact} was twofold lower for ACP-5862 compared with acalabrutinib (Table 2). The fit of ACP-5862 covalently bound to BTK was assessed in silico (Fig. 3), which showed the extent of folding required of the ring-opened ketone/amide of the metabolite for the binding of the electrophile. The second-order rate constants (k_{inact}/K_I) showed a twofold higher overall potency for acalabrutinib compared with ACP-5862, whereas ibrutinib and zanubrutinib covalent binding efficiency showed approximately 10-fold greater k_{inact}/K_I values (Table 2).

TABLE 1

Potency of acalabrutinib and ACP-5862 on kinases with a cysteine in the same position as Cys481 in BTK

Mean ± S.D. from at least three independent assay runs. Ibrutinib and zanubrutinib data included as points of reference to marketed, selective BTK inhibitors.

	IC50 (nM)			
Kinase	Acalabrutinib[d]	ACP-5862	Ibrutinib	Zanubrutinib
BTK[a]	5.1 ± 1.0	5.0 ± 1.0	1.5 ± 0.2	0.5 ± 0.0
TEC[b]	126 ± 11	345 ± 34	10 ± 12	44 ± 19
ITK[a]	>1000	>1000	4.9 ± 1.2	50 ± 5
BMX[c]	46 ± 12	15 ± 2.0	0.8 ± 0.1	1.4 ± 0.4
TXK[c]	368 ± 141	567 ± 174	2.0 ± 0.3	2.2 ± 0.6
EGFR[c]	>1000	>1000	5.3 ± 1.3	21 ± 1
ERBB2[c]	~1000	552 ± 166	6.4 ± 1.8	88 ± 26
ERBB4[c]	16 ± 5.0	343 ± 23	3.4 ± 1.4	6.9 ± 0.6
BLK[c]	>1000	>1000	0.1 ± 0.0	2.5 ± 0.4
JAK3[c]	>1000	>1000	32 ± 15	>1000

[a] Values from IMAP assay.
[b] Values from LanthaScreen assay.
[c] Values from Thermo Fisher using the Ź-LYTE assay.
[d] Results from a previous study (Barf et al., 2017; Kaptein et al., 2018).

In addition to BTK, there are nine other kinases that have a cysteine nucleophile in the same position as Cys481 in BTK: TEC, ITK, BMX, TXK, EGFR, ERBB2, ERBB4, BLK, and JAK3 (Barf and Kaptein, 2012). The potency of acalabrutinib and ACP-5862 was compared across a panel of kinases to which both may bind covalently (Table 1). Both acalabrutinib and ACP-5862 displayed IC_{50} values $>$ 100 nM for all off-target kinases except BMX (neither compound) and ERBB4 (ACP-5862 only). To compare potential differences in selectivity, the ratio of the IC_{50} for the respective kinases versus the IC_{50} for BTK was calculated (Supplemental Table 1). Relative selectivity data show that ACP-5862 was threefold less selective than acalabrutinib against BMX and the only kinase with less than 10-fold selectivity versus BTK (selectivity values are provided in Supplemental Table 1). For ERBB4, the other kinase for which acalabrutinib showed less than 10-fold selectivity versus BTK, ACP-5862 was approximately 20-fold more selective than acalabrutinib. The IC_{50} values for TEC and TXK for ACP-5862 showed approximately three- and twofold greater relative selectivity, respectively, than the parent. When comparing the fold selectivity versus BTK, the metabolite ACP-5862, like the parent acalabrutinib, showed a superior relative selectivity profile compared with ibrutinib and zanubrutinib for the other kinases in this panel. For ibrutinib, all IC_{50}s in this panel were less than or equal to 10 nM, and for zanubrutinib, all IC_{50} values in this panel were less than

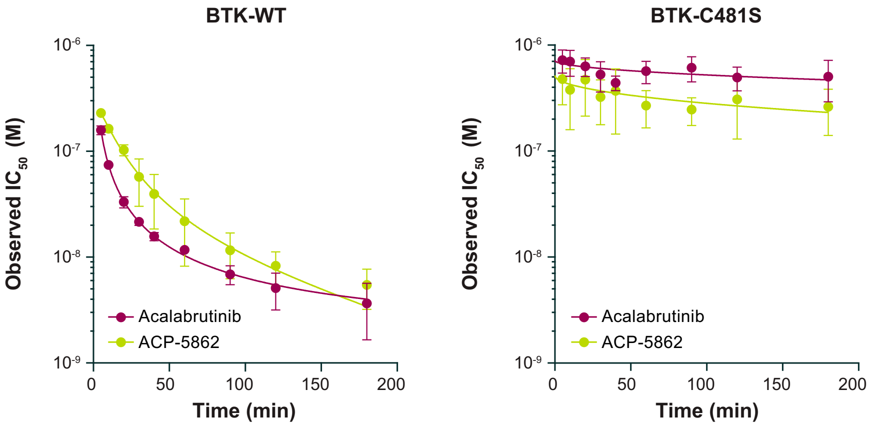

Fig. 2. IC$_{50}$ measurements over time for acalabrutinib and its major metabolite (ACP-5862) following incubation with BTK-WT or BTK-C481S, using the BTK LanthaScreen assay.

100 nM, except JAK3, resulting in lower selectivity relative to their respective BTK potencies.

In addition, the overall kinase selectivity profile was investigated for ACP-5862 and compared with acalabrutinib and the two other approved BTK inhibitors, ibrutinib and zanubrutinib. Profiling of all compounds at a single concentration (1 μM) was conducted using a KINOMEscan assay (Fig. 4), avoiding dependence on ATP concentration or choice of substrate (Fabian et al., 2005; Smyth and Collins, 2009), and hit rates were calculated (Table 3). Acalabrutinib had the lowest hit rate at 1 μM among the three Food and Drug Administration–approved BTK inhibitors across a panel of approximately 400 nonmutant kinases. The hit rate observed for ACP-5862 is comparable to acalabrutinib, indicating a similarly high selectivity for BTK.

To further investigate potential differences in potency between acalabrutinib and ACP-5862, both were profiled head-to-head in human primary peripheral B cells, either using human PBMCs or human WB. Acalabrutinib and ACP-5862 inhibitory activity on BCR-mediated cell surface expression of CD69 on peripheral B cells in PBMCs and WB revealed a greater difference in potency between the metabolite and parent compound compared with the biochemical kinase assays (Table 4). ACP-5862 was seven- to ninefold less potent than acalabrutinib in the in vitro cellular assays. The differences in potency between acalabrutinib and ibrutinib or zanubrutinib were decreased in the WB assay relative to the biochemical kinases assays as all three compounds had EC$_{50}$ values less than 10 nM.

Identification of Enzymes Responsible for Acalabrutinib and ACP-5862 Metabolism. During GST reaction phenotyping, acalabrutinib was stable in incubations with cytosol, and there was little or no formation of M5 (GSH conjugate, ACP-5530), M7 (cysteinyl-glycine conjugate, ACP-5531), and M10 (cysteine conjugate, ACP-5461), except in the presence of the highest concentration of acalabrutinib evaluated (100 μM) and only with the addition of excess GSH (0.6 mM). In incubations of acalabrutinib with a panel of recombinant human GST enzymes (rGSTA1, A2, M1, M2, P1, and T1 at 0.5 mg protein per ml), the relative contributions by GST isoforms toward the loss of acalabrutinib observed were rGSTM2 > rGSTM1 ≫ rGSTA1 and rGSTA2 (38%, 34%, 16%, and 16%, respectively; data not shown).

NADPH-dependent consumption of both acalabrutinib and ACP-5862 were observed in pooled HLMs. In incubations with individually expressed P450 enzymes, the metabolism of acalabrutinib and ACP-5862 was predominantly mediated by CYP3A4. The addition of specific CYP3A inhibitors, ketoconazole and troleandomycin, had a substantial inhibitory effect on the metabolic consumption of acalabrutinib and ACP-5862 in HLMs (Fig. 5). Specific chemical inhibitors for CYP1A2, CYP2A6, CYP2B6, CYP2C8, CYP2C9, CYP2C19, CYP2D6, and CYP2E1 had minimal effect on the metabolic turnover of acalabrutinib and ACP-5862. These data suggest that CYP3A4/5 appear to be the major contributors to the P450-mediated metabolism of acalabrutinib and ACP-5862. The rates of formation of ACP-5862 following incubation of acalabrutinib with HLM and human recombinant CYP3A4 exhibited Michaelis-Menten kinetics (Fig. 6), and a single-enzyme model

TABLE 2

BTK inactivation kinetic parameters for acalabrutinib, ACP-5862, ibrutinib, and zanubrutinib

K_I and k_{inact} parameters derived from IC$_{50}$ values over time from BTK-WT LanthaScreen using methods described by Krippendorff et al. (2009).

Compound	K_I (nM)	k_{inact} (s^{-1})	k_{inact}/K_I ($M^{-1}s^{-1}$)
Acalabrutinib[a]	181 ± 14	0.0056 ± 0.0025	$3.1 \times 10^4 \pm 1.48 \times 10^4$
ACP-5862	188 ± 9.0	0.0031 ± 0.0003	$1.7 \times 10^4 \pm 0.08 \times 10^4$
Ibrutinib	54 ± 49	0.027 ± 0.025	$47.7 \times 10^4 \pm 1.48 \times 10^4$
Zanubrutinib	126 ± 59	0.033 ± 0.013	$27.9 \times 10^4 \pm 0.08 \times 10^4$

[a] Results from previous study (Barf et al., 2017) shown for comparison with its major metabolite.

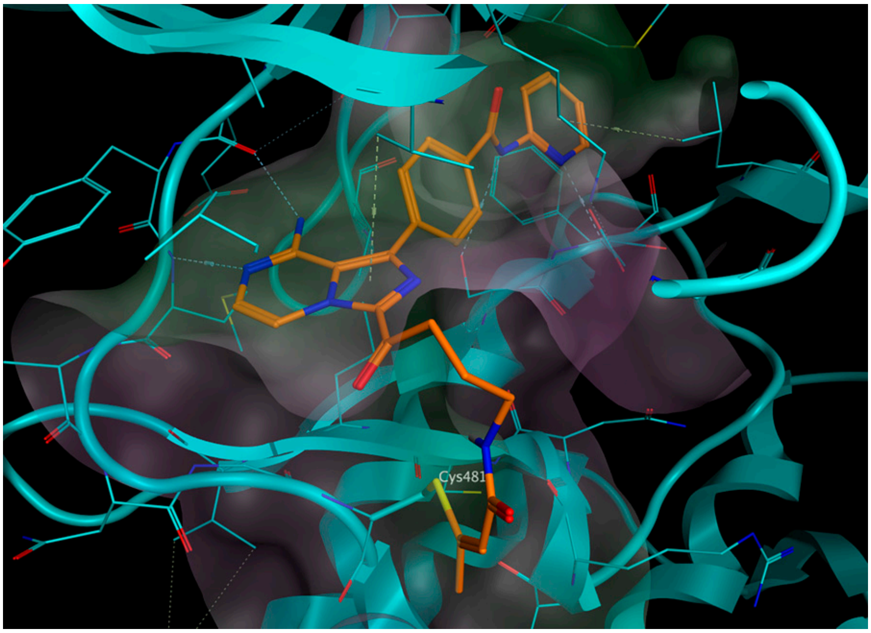

Fig. 3. Binding model of ACP-5862 in PDB 5P9J. Covalent docking was performed with Molecular Operating Environment (MOE, Chemical Computing Group, Montreal, Canada). Multiple docking poses were generated, and the one with the highest score is shown. The optimal docked pose illustrates the covalent interaction of the cysteinyl thiol of Cys-481 with the butynamide of ACP-5862.

was used to determine the K_m, 17.6 ± 1.8 and 2.78 ± 0.74 μM, and V_{max}, 920 ± 43 pmol/min per mg and 4.13 ± 0.23 pmol/min per pmol, values, respectively. The ACP-5862 (0.1 μM) half-life observed in HLM (0.5 mg/ml) was 58.7 minutes, and the calculated in vitro intrinsic clearance was 23.6 μl/min per mg.

UGT and P450 Inhibition by Acalabrutinib and ACP-5862. The inhibition of UGT1A1 and UGT2B7 activity by acalabrutinib or ACP-5862 was determined in HLMs (Supplemental Table 2). No inhibition of UGT1A1 and UGT2B7 activity was observed, with the exception of UGT1A1 inhibition

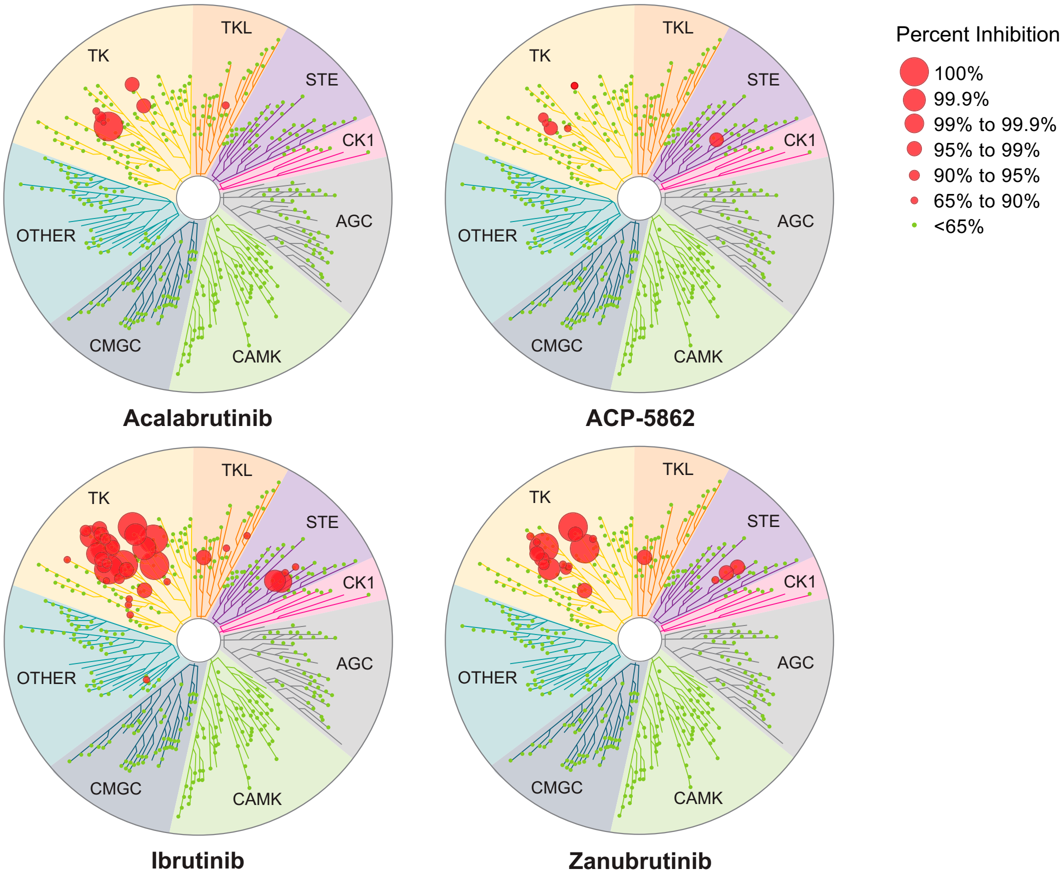

Acalabrutinib

ACP-5862

Ibrutinib

Zanubrutinib

Fig. 4. Comparison of acalabrutinib, ACP-5862, ibrutinib, and zanubrutinib (each at 1 μM) in competitive binding assays on wild-type and mutant kinases (KINOMEscan, DiscoverX, South San Francisco, CA). The size of the circles represents intervals of the percent inhibition versus the untreated control. For full quantitative details, refer to Table 3. Acalabrutinib and ibrutinib kinome maps reproduced with permission from Barf et al., (2017), Creative Commons license CC BY-NC 4.0 (https://creativecommons.org/licenses/by-nc/4.0/legalcode).

TABLE 3
Kinome profiling of BTK inhibitors using KINOMEscan at 1 μM

BTK Inhibitor (Total Number of Nonmutant Kinases Screened)	Number of Nonmutant Kinases Inhibited (Including BTK)		
	>65% Inhibition	>90% Inhibition	>99% Inhibition
Acalabrutinib (395)	7	4	1
ACP-5862[a] (403)	6	3	0
Ibrutinib (395)	37	25	13
Zanubrutinib[a] (403)	19	13	4

[a]Compared with the panel used for testing acalabrutinib and ibrutinib (conducted in 2014), eight additional nonmutant human kinases were added to the panel used for testing zanubrutinib and ACP-5862, conducted later. Zanubrutinib and ACP-5862 did not inhibit any of these kinases by >65%.

by ACP-5862, observed at 3 μM (34.7%), which was not sufficient to determine an IC_{50}.

The inhibition of individual P450 enzyme activities using selective substrates was evaluated in HLMs (Supplemental Table 2). Based on relevant US Food and Drug Administration–recommended calculations (https://www.fda.gov/regulatory-information/search-fda-guidance-documents/in-vitro-drug-interaction-studies-cytochrome-p450-enzyme-and-transporter-mediated-drug-interactions), acalabrutinib demonstrated weak inhibition of CYP2C8 (IC_{50} = 37 μM), CYP2C9 (IC_{50} = 28 μM), or CYP3A4/5 [IC_{50} = 57 μM (testosterone as substrate); IC_{50} = 69 μM (midazolam as substrate)]. In a similar manner, the metabolite ACP-5862 demonstrated limited inhibition of CYP2C9 (IC_{50} = 6.7 μM) and CYP2C19 (IC_{50} = 17 μM). Following a 30-minute preincubation of acalabrutinib with pooled HLMs in the presence of NADPH, a greater than 1.5-fold shift decrease in IC_{50} values was observed (Supplemental Table 2). Metabolism-dependent inhibition of CYP3A4/5 by acalabrutinib gave saturable inactivation rates, and k_{inact} and K_I values for inactivation of midazolam 1'-hydroxylation and testosterone 6β-hydroxylation were similar and measured to be 0.019 ± 0.001 and 0.018 ± 0.002 $minute^{-1}$ and 11 ± 2 and 9.2 ± 3.6 μM, respectively. Acalabrutinib showed little or no evidence of metabolism-dependent inhibition of CYP1A2, CYP2B6, CYP2C19, and CYP2D6. Time-dependent inhibition studies of CYP2C8, CYP2C9, and CYP3A4/5 by metabolite ACP-5862 in NADPH-fortified HLMs revealed a shift to lower IC_{50} values (Supplemental Table 2), indicating potential for metabolism-based inactivation of these isoforms. For the most sensitive enzyme, CYP2C8, the apparent metabolism-dependent inactivation had a measured k_{inact} value of 0.012 ± 0.003 $minute^{-1}$ and K_I value of 4.0 ± 2.5 μM.

P450 Induction by Acalabrutinib and ACP-5862. The potential for acalabrutinib and ACP-5862 to induce the expression of P450 enzymes was examined in primary cultures of freshly isolated human hepatocytes, each from three individual donors (data not shown). Under the conditions of the acalabrutinib study, where the positive controls caused anticipated and appropriate increases in P450 enzyme expression, the effect on CYP1A2 mRNA levels was greatest. Treatment of the cultured human hepatocytes from all three individuals with up to 50 μM acalabrutinib caused concentration-dependent increases (>2.0-fold and >20% of the positive control, up to 32.9-fold change). However, acalabrutinib caused an approximately two-fold and 5.8-fold induction of CYP1A2 mRNA at 1 and 5 μM, respectively, the latter having 15% of the effect of the positive control, omeprazole, which showed a 38-fold change in CYP1A2 mRNA. The increase observed in CYP2B6 and 3A4 mRNA levels at 50 μM acalabrutinib concentrations in at least one of the hepatocyte preparations tested was up to 2.9- and 2.44-fold, respectively (also >2.0-fold and/or ≥20% of the positive control). However, acalabrutinib caused little or no induction of CYP2B6 or CYP3A4 mRNA at 10 μM concentrations.

ACP-5862 caused no induction of CYP1A2 or CYP2B6 mRNA at 50 μM concentrations. ACP-5862 caused some modest induction of CYP3A4 mRNA (2.2- to 3.5-fold, which were 1.7% to 3.5% of positive control, 20 μM rifampicin) at 10 μM concentrations.

In Vitro Efflux and Uptake Transporter Inhibition. The potential for acalabrutinib and ACP-5862 to inhibit human P-gp transport across confluent monolayers of Caco-2 cells was assessed by measuring the basolateral-to-apical transport of the probe substrate digoxin (Table 5). Neither acalabrutinib nor ACP-5862 were potent inhibitors of P-gp digoxin transport in Caco-2 cells. Similarly, acalabrutinib and ACP-5862 were not potent inhibitors of BCRP evaluated in MDCKII cells by measuring their effect on the transport of prazosin (Table 5). Acalabrutinib and ACP-5862 were also assessed as inhibitors of the hepatic uptake transporters OATP1B1 and OATP1B3 in HEK293 cells (Supplemental Table 3). Acalabrutinib was not an inhibitor of OATP1B1 and OATP1B3. ACP-5862 only moderately inhibited OATP1B1 and OATP1B3. In addition, acalabrutinib and ACP-5862 were evaluated as inhibitors of the kidney uptake transporters OAT1, OAT3, and OCT2 in HEK293 cells (Supplemental Table 3). Acalabrutinib was not an inhibitor of OAT1 and only moderately inhibited OAT3 and OCT2. ACP-5862 was not a potent inhibitor of OAT1 or OCT2 and did not inhibit OAT3.

TABLE 4
Inhibition of BCR-mediated activation of human peripheral B cells by acalabrutinib and its major circulating metabolite, ACP-5862, using human PBMC and WB
Results are mean ± S.D. for four independent experiments using material from four donors.

Assay	EC_{50} (nM)			
	Acalabrutinib	ACP-5862	Ibrutinib	Zanubrutinib
hPBMC: anti-IgM–induced CD69	2.9 ± 0.2	26 ± 16	0.6 ± 0.0	0.9 ± 0.3
hWB: anti-IgD–induced CD69	9.2 ± 4.4	64 ± 6	5.8 ± 3.0	2.4 ± 0.4

CD, clusters of differentiation; H, human; hPBMC, human PBMC; hWB, human WB; IgM, anti-immunoglobulin M.

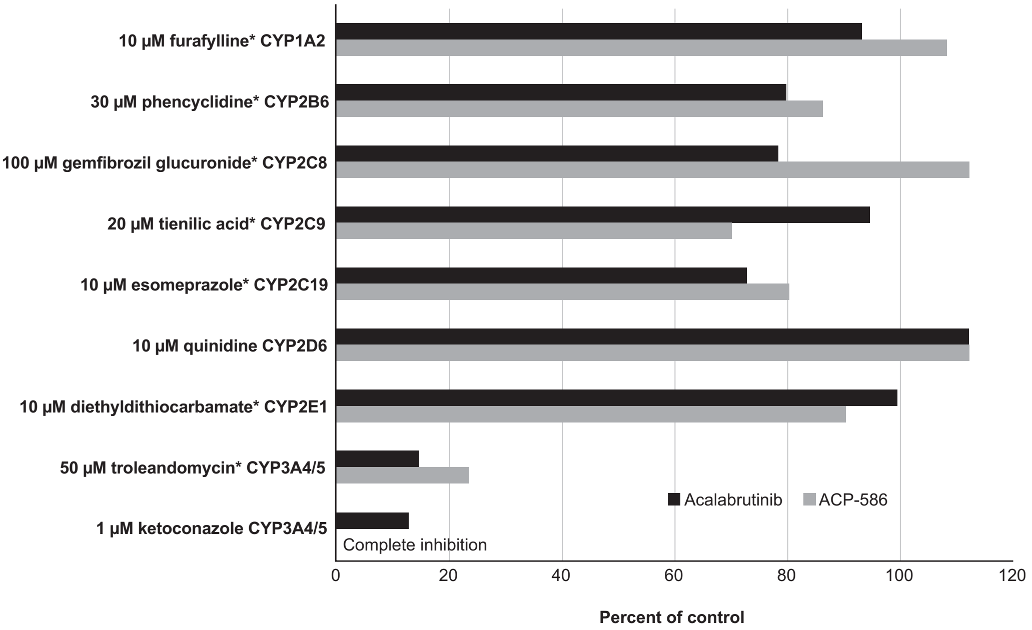

Fig. 5. Effect of P450 isoform-selective chemical inhibitors on the disappearance of acalabrutinib and ACP-5862 in human liver microsomes. *, metabolism-dependent chemical inhibitors.

Finally, similar tests of MATE1 and MATE2-K in HEK293 cells revealed potent inhibition of MATE1 by ACP-5862 (Supplemental Table 3).

Transporter Substrate Assays. The bidirectional permeability of acalabrutinib or ACP-5862 was assessed in MDCKII-P-gp and MDCKII-BCRP cell monolayers to determine their potential to be substrates of P-gp or BCRP in the presence and absence of selective inhibitors (Table 6). Acalabrutinib and ACP-5862 were good substrates for P-gp, and transport for both was strongly inhibited in the presence of a multidrug resistance protein 1 inhibitor, valspodar. The efflux ratios for both acalabrutinib and ACP-5862 were also indicative of being substrates for BCRP and were similarly inhibited by the BCRP inhibitor Ko143.

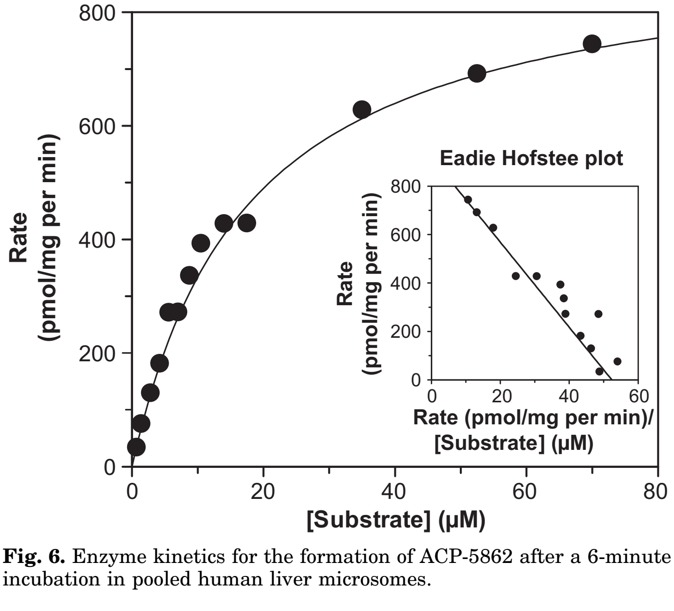

Fig. 6. Enzyme kinetics for the formation of ACP-5862 after a 6-minute incubation in pooled human liver microsomes.

The cellular uptake of acalabrutinib or ACP-5862 was assessed in cells transfected with hepatic uptake transporters OATP1B1 or OATP1B3 or vector control. The maximum influx uptake ratio for acalabrutinib observed with OATP1B1 was 1.44, and that for ACP-5862 was 1.66. The maximum uptake ratio for acalabrutinib observed with OATP1B3 was 0.918. The uptake ratio for ACP-5862 was generally <2, and for the instances in which the uptake ratio was near 2, the uptake was not reduced by the presence of rifampicin (10 µM) as inhibitor (data not shown). These data indicate that acalabrutinib and ACP-5862 are not substrates of OATP1B1 and OATP1B3. The cellular uptake of acalabrutinib was similarly assessed in cells transfected with renal uptake transporters. The maximum influx uptake ratio for acalabrutinib observed with OAT1 was 1.26, and that for OAT3 was 1.83. OAT3 acalabrutinib uptake was time-dependent and was reduced in the presence of the OAT3 inhibitor probenecid, suggesting acalabrutinib interacts with OAT3; however, the uptake ratios compared with control cells were <2 at all concentrations tested, suggesting acalabrutinib is not a substrate of OAT3 (data not shown). The maximum influx rate ratio for acalabrutinib observed with OCT2 was 1.85. These data collectively indicate that acalabrutinib is not a substrate of OAT1, OAT3, and OCT2.

Acalabrutinib Metabolite Generation by HLMs. Extracts from [^{14}C]acalabrutinib (10 µM, MH^{+}466) incubations with HLMs and NADPH were analyzed by radiochromatography and LC-MS using a previously described HPLC method (Podoll et al., 2019). Two prominent metabolites were observed that eluted near the parent molecule (40 minutes). The earlier peak at approximately 38 minutes had a protonated molecular ion at m/z 464 that matched the retention time and mass of previously characterized M25 and accounted for approximately 15% of the total radioactivity in the trace. At 2 mass units lower than the parent molecule, the fragmentation pattern was diagnostic for a dehydrogenation or hydroxylation-

TABLE 5
Efflux transporter inhibition by acalabrutinib and ACP-5862

		Acalabrutinib		ACP-5862	
		I_{max} = 1.45 μM; $I_{max,u}$ = 0.036 μM		I_{max} = 0.84 μM; $I_{max,u}$ = 0.012 μM	
Transporter	Substrate	IC_{50} (μM)	Static Model Interpretation Potential for Clinical (Yes/No)	IC_{50} (μM)	Static Model Interpretation Potential for Clinical (Yes/No)
P-gp	Digoxin	98.3	[a]Gut: No; [b]Systemic: No	>20	[b]Systemic: No
BCRP	Prazosin	9	[a]Gut: Yes; [b]Systemic: No	6.0	[b]Systemic: No

For interpretation $IC_{50} = K_i$; [a]I_{gut} = dose/250 ml = 860 μM; if $K_i \leq 0.1 \times I_{gut}$, then yes; [b]if $K_i < 50 \times I_{max,u}$, then yes. (https://www.fda.gov/regulatory-information/search-fda-guidance-documents/in-vitro-drug-interaction-studies-cytochrome-p450-enzyme-and-transporter-mediated-drug-interactions)
BI_{gut}, intestinal luminal concentration; $I_{max,u}$, maximal unbound plasma concentration.

dehydration within the pyrrolidine ring. Fragment ions at m/z 370 and 342 were supportive of the assigned structure, and an ion at m/z 239 placed the loss of 2 mass units in the pyrrolidine ring (Fig. 7A) via a neutral loss of 134 mass units from the ion at m/z 370. NMR characterization was required to establish the position of the double bond in the dihydropyrrole ring (Fig. 8).

The second prominent metabolite observed in HLMs, M27, eluted after parent drug at approximately 44 minutes with a +16 Da protonated molecular ion at m/z 482 and accounted for approximately 50% of the total radioactivity in the chromatogram. Following purification by semipreparative HPLC and fraction collection, the isolated biosynthetic metabolite matched the retention time and mass of the initial incubation extract and (as determined later) matched the synthetic standard ACP-5862.

Unlike putative carbinolamide metabolites that would be formed by hydroxylation of the 2- or 5-carbons of the acalabrutinib pyrrolidine ring, hydroxy metabolites of the 3- and 4-positions were expected to be stable. Enantiomers of putative 3- and 4-hydroxypyrrolidine metabolites were synthesized for comparison with M27. All four synthetic compounds eluted earlier than M27 at less than 35 minutes (Supplemental Fig. 1) and had a protonated molecular ion at m/z 482. The fragmentation diagnostic for stable 3- and 4-hydroxylated pyrrolidine standards included fragment ions m/z 152 and 86, which were also observed for the late-eluting M27 peak (Fig. 7B). Ultimately, NMR spectroscopy was required to define the structure of M27.

Structural Elucidation of M25 and M27 by NMR. Details of the NMR results can be found in the Supplemental Results, Supplemental Figs. 2–10, and Supplemental Tables 4–6. Briefly, the analysis focused on the aliphatic regions of the spectra of M25 and M27, which were compared with prior data available for acalabrutinib. For M25, the aliphatic region revealed a splitting of the methyl protons at the end of the butynamide into two singlets (Supplemental Table 4). This was similarly found in the aliphatic region of the acalabrutinib proton NMR and ascribed to a conformational exchange around the amide bond in the intact pyrrolidine ring. In contrast, there was no evidence of inversion in the NMR of M27, wherein all three protons were ascribed to one singlet (Supplemental Fig. 6; Supplemental Table 5). Additionally, the M27 NMR revealed that the triplet, quintet, triplet proton splitting pattern of three isolated, contiguous, and freely rotating methylene groups was present, also consistent with the opening of the pyrrolidine ring. Finally, a ^{1}H–^{13}C 2/3-bond correlation experiment (Fig. 9) showed coupling between protons labeled H_b and H_c with an adjacent carbonyl carbon at 191 ppm. Overall, ^{1}H NMR and ^{1}H-^{13}C correlation spectra indicated an acalabrutinib biotransformation mechanism wherein hydroxylation of the chiral benzylic carbon between the fused imidazole-pyrazine ring system and the pyrrolidine ring nitrogen affords an unstable carbinolamide intermediate. The carbinolamide undergoes spontaneous ring opening to the keto-amide major metabolite (M27) or dehydration to the

TABLE 6
Efflux transporter substrate determination: bidirectional permeability of acalabrutinib and ACP-5862 across MDCKII cells
P-gp positive control was digoxin, and BCRP positive control was prazosin. Data are the mean ± S.D. of triplicate determinations.

	Acalabrutinib as Substrate				ACP-5862 as Substrate			
		P_{app} (×10^{-6} cm/sec)				P_{app} (×10^{-6} cm/sec)		
MDCKII Cell Line	Substrate Concentration (μM)	Apical to Basal	Basal to Apical	Efflux Ratio	Substrate Concentration (μM)	Apical to Basal	Basal to Apical	Efflux Ratio
P-gp	1	1.86 ± 0.20	78.8 ± 3.2	42.4	2	NA	60.3 ± 6.4	NC
	10	2.22 ± 0.09	80.7 ± 1.1	36.4	10	1.15 ± 0.00	65.4 ± 5.4	57.0
	30	1.96 ± 0.13	56.3 ± 0.8	28.7	50	2.28 ± 0.06	87.2 ± 6.2	38.3
	1 (+10 μM valspodar)	24.1 ± 1.1	22.6 ± 1.6	0.935	2 (+10 μM valspodar)	13.5 ± 1.8	27.8 ± 2.0	2.05
	10 (+10 μM valspodar)	18.0 ± 1.0	22.2 ± 1.6	1.24	10 (+10 μM valspodar)	15.3 ± 1.2	29.2 ± 2.9	1.92
	30 (+10 μM valspodar)	16.5 ± 0.3	16.6 ± 1.7	1.01	50 (+10 μM valspodar)	23.7 ± 1.6	36.0 ± 4.1	1.52
BCRP	1	8.53 ± 0.49	54.2 ± 1.2	6.36	2	4.67 ± 0.08	57.7 ± 1.3	12.3
	3	5.36 ± 0.22	45.2 ± 2.4	8.44	10	6.01 ± 0.16	61.2 ± 1.8	10.2
	10	5.92 ± 0.38	48.7 ± 1.9	8.23	50	22.9 ± 1.0	74.0 ± 4.8	3.23
	1 (+1 μM Ko143)	19.0 ± 1.9	42.9 ± 8.7	2.25	2 (+1 μM Ko143)	24.5 ± 1.2	44.1 ± 1.7	1.80
	3 (+1 μM Ko143)	15.4 ± 1.3	35.0 ± 6.6	2.27	10 (+1 μM Ko143)	30.8 ± 1.5	40.6 ± 1.8	1.32
	10 (+1 μM Ko143)	16.9 ± 1.6	36.9 ± 8.5	2.18	50 (+1 μM Ko143)	46.2 ± 2.3	49.4 ± 3.7	1.07

NC, not counted; P_{app}, apparent permeability.

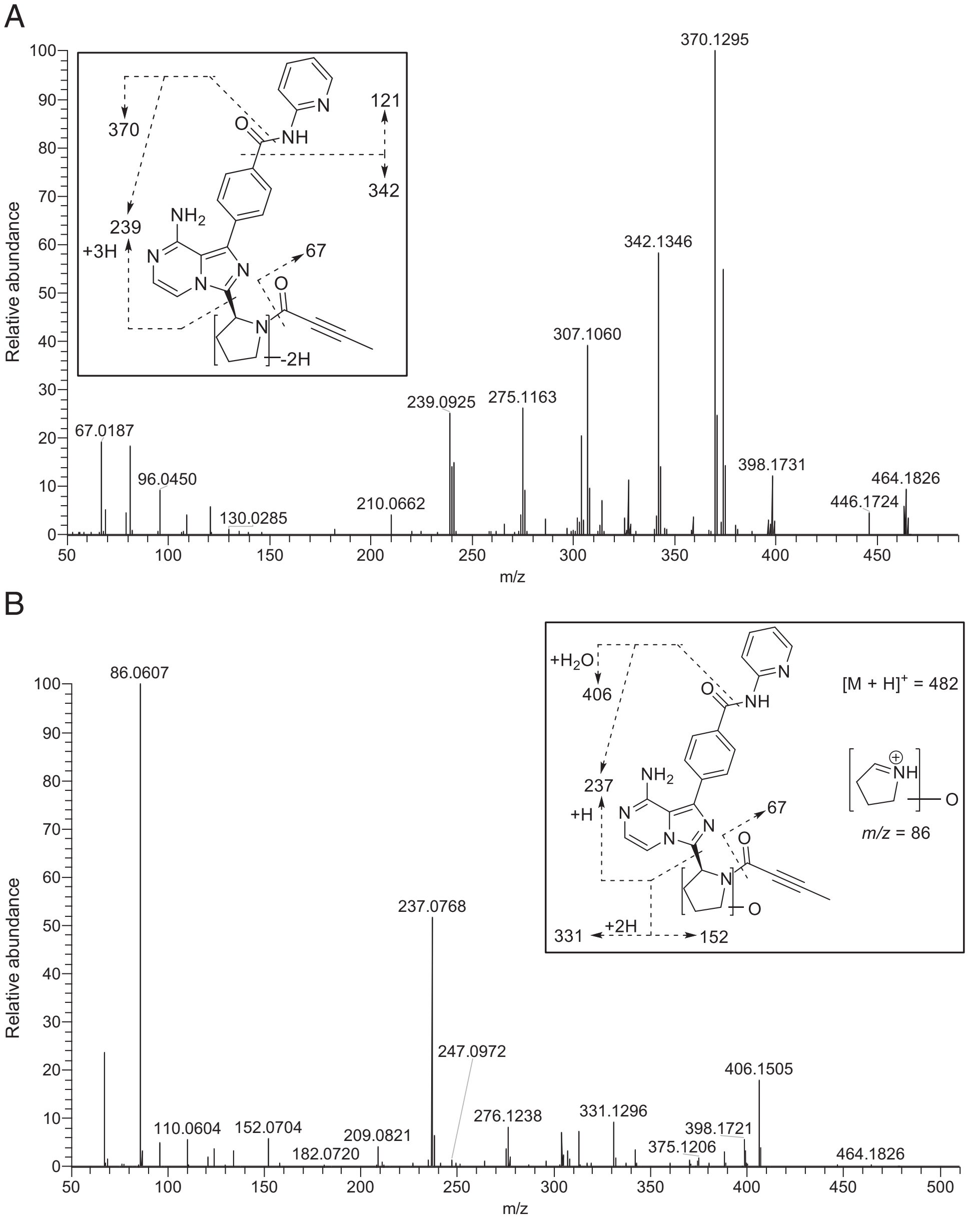

Fig. 7. Product ion mass spectra of metabolites (A) M25 (m/z 464) and (B) M27 (m/z 482) from analysis of a 0- to 6-hour AUC pooled plasma sample obtained from a patient following repeat oral doses of acalabrutinib (100 mg).

unsaturated, dihydropyrrole M25 (Fig. 8). Taken together, the structure of metabolites M25 and M27 triangulate back to the common carbinolamide intermediate. The structure of M27 was ultimately confirmed by comparison of the NMR data to those of a synthetic standard (ACP-5862).

Discussion

ACP-5862 is a major metabolite of acalabrutinib that was previously observed to have systemic exposure, which justified testing whether it could contribute to the pharmacological activity of acalabrutinib therapy (Podoll et al., 2019). In this work, we further elucidated the structure of ACP-5862 as a pyrrolidine ring–opened ketone/amide that was rapidly formed and metabolized by CYP3A. The butynamide warhead was retained, and the metabolite demonstrated intrinsic activity against BTK similar to the parent molecule. The ACP-5862 primary pharmacology data were consistent with a covalent mechanism of action, demonstrated activity in cellular assays, and a selectivity profile similar to that of acalabrutinib. Taken together, these findings suggest the potential for a clinically relevant pharmacological effect by ACP-5862.

Acalabrutinib and ACP-5862 have similar overall kinase selectivity profiles and are more selective for BTK compared with ibrutinib and zanubrutinib (Fig. 4). This was demonstrated using a competitive binding assay (Fabian et al., 2005), which avoids the dependency of the assay on ATP concentration or choice of substrate as seen in previous comparisons (Guo et al., 2019; Shadman et al., 2021). The lowest overall kinase hit rates were observed for acalabrutinib and ACP-5862 when compared with ibrutinib and zanubrutinib, indicating no

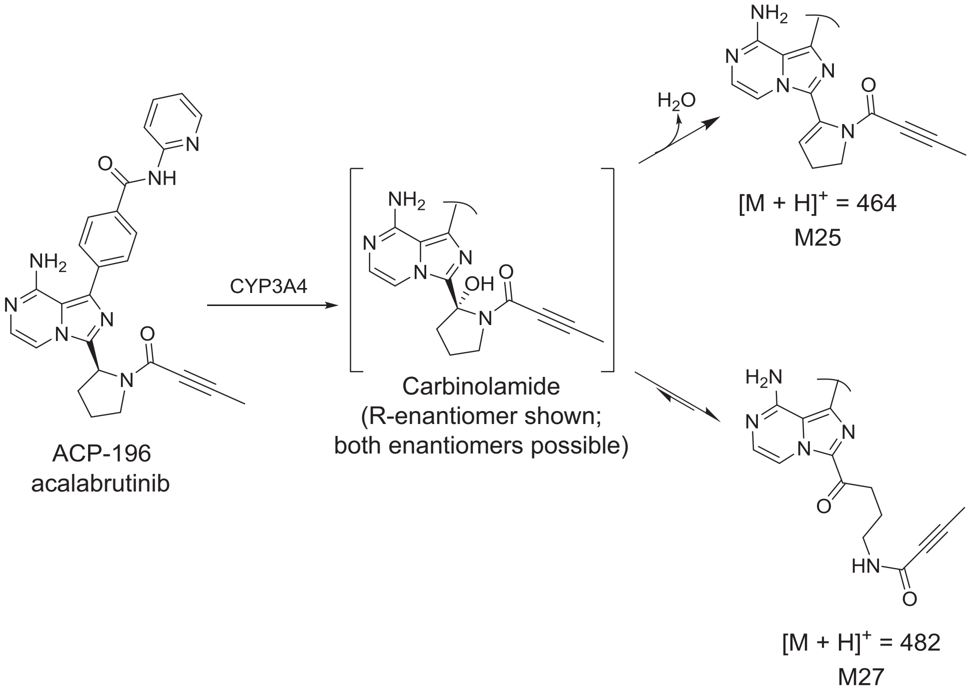
NH
N
O
NH$_2$
N
N
N
N
O
ACP-196
acalabrutinib
CYP3A4
NH$_2$
OH
O
Carbinolamide
(R-enantiomer shown;
both enantiomers possible)
H$_2$O
NH$_2$
O
[M + H]$^+$ = 464
M25
H$_2$N
O
HN
O
[M + H]$^+$ = 482
M27

Fig. 8. Oxidative metabolic pathway to major active metabolite ACP-5862 (M27).

loss in selectivity for the major metabolite (Table 3). Similar selectivity for BTK over other kinases having Cys in the same position as the Cys481 residue in BTK was observed for parent and metabolite (Table 1), with ACP-5862 being slightly more potent on BMX and acalabrutinib more potent on ERBB4. The structural features of acalabrutinib that are retained in ACP-5862, including retention of the ATP binding site recognition of the imidazopyridine core and the butynamide warhead of acalabrutinib, impart the selectivity advantage of the parent molecule onto the metabolite compared with the acryloyl warhead–containing BTK inhibitors ibrutinib and zanubrutinib.

This is confirmed when looking at the fold selectivity versus BTK for the panel of kinases with potential for covalent binding. Both acalabrutinib and ACP-5862 showed an enhanced selectivity versus BTK for this kinase panel compared with

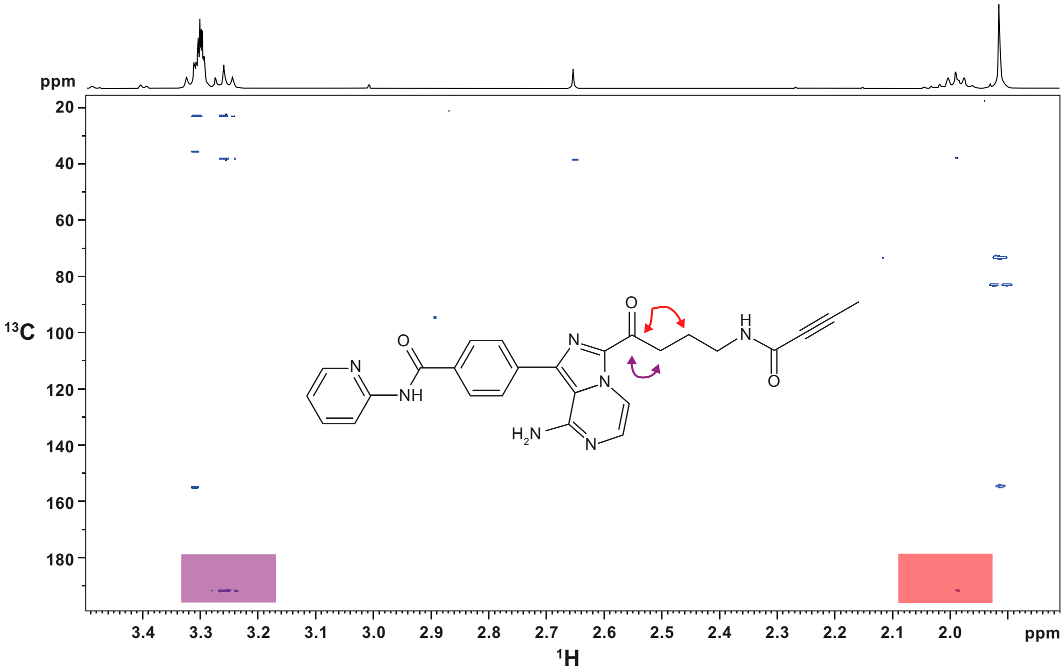

Fig. 9. An expanded aliphatic region of the ^{1}H–^{13}C gradient selected heteronuclear 2/3-bond correlation NMR spectrum of acalabrutinib metabolite M27 (ACP-5862).

ibrutinib and zanubrutinib. Affinity is not the only criterion for selectivity, and inclusion of both acalabrutinib and ACP-5862 inactivation kinetics may be required to fully assess acalabrutinib's relative selectivity among covalent inhibitor therapies (Hopper et al., 2020).

The difference in inhibition potency (IC_{50}) over time between BTK-WT and BTK-C481S (Fig. 2) indicated that both acalabrutinib and ACP-5862 bind covalently to Cys481 in the ATP binding site of BTK. The nonlinear time-dependent decrease in IC_{50} observed in BTK-WT reflects the time-dependent loss of BTK activity, typically observed for targeted covalent inhibitors under saturating conditions (Krippendorff et al., 2009). The serine residue in the mutant form of BTK with Cys481Ser no longer serves as a nucleophile for the covalent binding, and the modest inhibition observed reflects the reversible interaction of acalabrutinib and metabolite with BTK. These combined results are in line with a shared mechanism of BTK inhibition for both ACP-5862 and acalabrutinib—covalent binding to Cys481. The BTK inactivation rate (k_{inact} of ACP-5862 was twofold lower than that of acalabrutinib (Table 2) (Barf et al., 2017), which may be influenced by metabolic oxidation and opening of the pyrrolidine ring. The low flexibility between the electrophile and the imidazopyridine core in acalabrutinib provides the optimal geometry for rapid bond formation (Liu et al., 2013). In silico docking of ACP-5862 in the active site of BTK is consistent with covalent binding to Cys481 (Fig. 3). Increased flexibility of the linear butanoyl electrophile, and potentially reduced reactivity of the butynamide moiety, may explain the twofold lower k_{inact} value of ACP-5862 compared with acalabrutinib.

Comparison of the inactivation kinetics between the acrylamide- and butynamide-containing covalent inhibitors is consistent with their anticipated relative reactivity. The k_{inact}/K_I values for ibrutinib and zanubrutinib are approximately an order of magnitude higher than acalabrutinib and ACP-5862 (Table 2), indicating higher efficiency of covalent bond formation by the more reactive acrylamide. The k_{inact}/K_I defines the relationship between the rate of bond formation, time, and the inhibitor concentration (Strelow, 2017). Model-derived estimates of occupancy based on the k_{inact}/K_I and unbound area under the curve (AUC) of a covalent inhibitor show that concentrations at and above its K_I do not meaningfully increase inactivation rates. Simultaneously, higher inhibitor concentrations decrease the selectivity for the intended target (Strelow, 2017). Strelow (2017) concludes that covalent kinase inhibitors may be dosed at levels that minimize inactivation of off-target kinases by balancing the unbound AUC with the k_{inact}/K_I to optimize for the targeted kinase. Acalabrutinib is dosed to achieve exposures necessary for prolonged target coverage (BTK occupancy). When the total active moiety [acalabrutinib (100 mg twice daily) plus ACP-5862 steady-state plasma concentrations] is considered, the exposure achieved is comparable to that of ibrutinib (560 mg daily) and zanubrutinib (160 mg twice daily) alone, all at doses that have high clinical BTK occupancy (≥95%) (Edlund et al., 2022b). In the case of acala-brutinib, additional exposure to the metabolite may have provided prolonged BTK occupancy over the treatment interval at a lower dose than with acalabrutinib alone.

Because assay conditions in biochemical kinase assays affect potency (ATP concentration, kinase concentration, incubation time, etc.), comparison of potency was also conducted using cellular assays. When examining inhibition of BCR-stimulated peripheral B cells of healthy individuals, using either human PBMCs or human WB, ACP-5862 was seven- to ninefold less potent than acalabrutinib (Table 4). Ibrutinib and zanubrutinib showed an EC_{50} of 5.8 and 2.4 nM, respectively, in human WB, in line with previously reported data (Guo et al., 2019). Fully reversible inhibitors that show potency differences in static, cellular in vitro systems can be influenced by differences in free fraction, or cellular partitioning, and the free fraction of ACP-5862 is approximately half that of acalabrutinib (Podoll et al., 2019). However, although the initial binding kinetics may be influential, the steady-state in vivo efficacy for an irreversible inhibitor is not determined by free drug concentrations (Smith et al., 2010). The actual contribution of the ACP-5862 metabolite to clinical efficacy in humans cannot be discerned from BTK occupancy data since the assay does not distinguish between BTK bound to parent versus that to metabolite. Yet, findings from a published exposure-response analysis demonstrated similar efficacy results when assessed as a function of acalabrutinib and ACP-5862 exposure (AUC and C_{max}) (Edlund et al., 2022b). The totality of the exposure and activity data denote a secondary role of the active metabolite ACP-5862 relative to the parent drug (Podoll et al., 2019).

No dose modifications with cytochrome P450 substrates are required for acalabrutinib and ACP-5862 as perpetrators based on in vitro IC_{50} values and clinical levels (https://den8dhaj6zs0e.cloudfront.net/50fd68b9-106b-4550-b5d0-12b045f8b184/61cc04a6-2b15-49f0-a896-192e8462ef3d/61cc04a6-2b15-49f0-a896-192e8462ef3d_viewable_rendition__v.pdf). Both are eliminated by CYP3A4, reducing the chance that the sum of the total active moieties would become the victim of CYP3A inhibitors or inducers. The Cl_{int} of acalabrutinib, 52.3 μl/min per mg for ACP-5862 product formation (V_{max}/K_m), was greater than the Cl_{int} of ACP-5862 metabolic clearance in HLM. These data are in agreement with clinical studies, which showed the half-life and AUC of ACP-5862 were approximately twofold higher than acalabrutinib in healthy subjects and cancer patients (Zhou et al., 2019; Edlund et al., 2022b). The effects of CYP3A inhibitors on acalabrutinib PK were evaluated in a previous study using a physiologically based pharmacokinetic model, taking into account effects on both parent and metabolite (Zhou et al., 2019). These findings were confirmed during acalabrutinib clinical evaluations as a victim with CYP3A inhibitors, which ultimately influence dose recommendations (Chen et al., 2022). This substantiates the reported data and reinforces the importance of considering all pharmacologically active entities with acalabrutinib therapy. PK of substrates of most transporters also are not likely to be altered by acalabrutinib or ACP-5862 (Supplemental Table 3). Static PK model calculations indicated modest increases in exposure to coadministered BCRP substrates via inhibition of intestinal BCRP (acalabrutinib) or renal MATE1 (ACP-5862). However, based on exposure relative to clinically impactful MATE1 inhibitors (Hibma et al., 2016; Zamek-Gliszczynski et al., 2018), this was not expected to be clinically actionable.

The prior study revealed the structure of the ACP-5862 to be a pyrrolidine ring that was oxidized at 1 of 5 positions, but full characterization was not achieved (Podoll et al., 2019). The 2-position oxidation to a carbinolamide, and its ring-opened ketone/amide congener, was proven with the NMR spectra of the biosynthetic and synthetic reference samples. The 2 position was the biotransformation most likely to result in a metabolite less polar than the parent drug (Fig. 8). The

M25 metabolite was also isolated, purified, and characterized by NMR to unambiguously assign both structures (Fig. 9; Supplemental Figs. 2–10; Supplemental Tables 1–3).

In conclusion, this work characterized the structure and biologic activity of ACP-5862, the major metabolite of acalabrutinib. The current data suggest that ACP-5862 may be clinically relevant to the efficacy of acalabrutinib therapy while retaining any potential benefits of high BTK selectivity.

Acknowledgments

The authors thank the staff of XenoTech, LLC for their performance and reporting of the GST, P450, and transporter in vitro drug interaction experiments. Editorial assistance, funded by AstraZeneca, was provided by Allison Green and Cynthia Gobbel of Peloton Advantage, LLC, an OPEN Health company.

Authorship Contributions

Participated in research design: Podoll, Pearson, Kaptein, Evarts, de Bruin, Fretland, Barf, Slatter.

Conducted experiments: de Bruin, Emmelot-van Hoek, de Jong, van Lith, Sun, Byard, Hoogenboom.

Performed data analysis: Podoll, Pearson, Kaptein, Evarts, de Bruin, Emmelot-van Hoek, de Jong, van Lith, Sun, Byard, Fretland, Hoogenboom, Barf, Slatter.

Wrote or contributed to the writing of the manuscript: Podoll, Pearson, Kaptein, Evarts, de Bruin, Emmelot-van Hoek, de Jong, van Lith, Sun, Byard, Fretland, Hoogenboom, Barf, Slatter.

References

Baillie TA (2016) Targeted covalent inhibitors for drug design. *Angew Chem Int Ed Engl* **55**:13408–13421.

Baillie TA, Cayen MN, Fouda H, Gerson RJ, Green JD, Grossman SJ, Klunk LJ, LeBlanc B, Perkins DG, and Shipley LA (2002) Drug metabolites in safety testing. *Toxicol Appl Pharmacol* **182**:188–196.

Barf T, Covey T, Izumi R, van de Kar B, Gulrajani M, van Lith B, van Hoek M, de Zwart E, Mittag D, Demont D, et al. (2017) Acalabrutinib (ACP-196): A covalent Bruton tyrosine kinase inhibitor with a differentiated selectivity and in vivo potency profile. *J Pharmacol Exp Ther* **363**:240–252.

Barf T and Kaptein A (2012) Irreversible protein kinase inhibitors: balancing the benefits and risks. *J Med Chem* **55**:6243–6262.

Brouwer KL, Keppler D, Hoffmaster KA, Bow DA, Cheng Y, Lai Y, Palm JE, Stieger B, and Evers R; International Transporter Consortium (2013) In vitro methods to support transporter evaluation in drug discovery and development. *Clin Pharmacol Ther* **94**:95–112.

Byrd JC, Harrington B, O'Brien S, Jones JA, Schuh A, Devereux S, Chaves J, Wierda WG, Awan FT, Brown JR, et al. (2016) Acalabrutinib (ACP-196) in relapsed chronic lymphocytic leukemia. *N Engl J Med* **374**:323–332.

Chandrasekaran A, Shen L, Lockhead S, Oganesian A, Wang J, and Scatina J (2010) Reversible covalent binding of neratinib to human serum albumin in vitro. *Drug Metab Lett* **4**:220–227.

Chen B, Zhou D, Wei H, Yotvat M, Zhou L, Cheung J, Sarvaria N, Lai R, Sharma S, Vishwanathan K, et al. (2022) Acalabrutinib CYP3A-mediated drug-drug interactions: Clinical evaluations and physiologically based pharmacokinetic modelling to inform dose adjustment strategy. *Br J Clin Pharmacol* **88**:3716–3729.

Dickinson PA, Cantarini MV, Collier J, Frewer P, Martin S, Pickup K, and Ballard P (2016) Metabolic disposition of osimertinib in rats, dogs, and humans: insights into a drug designed to bind covalently to a cysteine residue of epidermal growth factor receptor. *Drug Metab Dispos* **44**:1201–1212.

Edlund H, Bellanti F, Liu H, Vishwanathan K, Tomkinson H, Ware J, Sharma S, and Buil-Bruna N (2022a) Improved characterization of the pharmacokinetics of acalabrutinib and its pharmacologically active metabolite, ACP-5862, in patients with B-cell malignancies and in healthy subjects using a population pharmacokinetic approach. *Br J Clin Pharmacol* **88**:846–852.

Edlund H, Buil-Bruna N, Vishwanathan K, Wei H, Raman R, de Kock M, He Z, Liu H, Baek M, Ware J, et al. (2022b) Exposure-response analysis of acalabrutinib and its active metabolite, ACP-5862, in patients with B-cell malignancies. *Br J Clin Pharmacol* **88**:2284–2296.

Edlund H, Lee SK, Andrew MA, Slatter JG, Aksenov S, and Al-Huniti N (2019) Population pharmacokinetics of the BTK inhibitor acalabrutinib and its active metabolite in healthy volunteers and patients with B-cell malignancies. *Clin Pharmacokinet* **58**:659–672.

Fabian MA, Biggs 3rd WH, Treiber DK, Atteridge CE, Azimioara MD, Benedetti MG, Carter TA, Ciceri P, Edeen PT, Floyd M, et al. (2005) A small molecule-kinase interaction map for clinical kinase inhibitors. *Nat Biotechnol* **23**:329–336.

Guo Y, Liu Y, Hu N, Yu D, Zhou C, Shi G, Zhang B, Wei M, Liu J, Luo L, et al. (2019) Discovery of zanubrutinib (BGB-3111), a novel, potent, and selective covalent inhibitor of Bruton's tyrosine kinase. *J Med Chem* **62**:7923–7940.

Herman SEM, Montraveta A, Niemann CU, Mora-Jensen H, Gulrajani M, Krantz F, Mantel R, Smith LL, McClanahan F, Harrington BK, et al. (2017) The Bruton Tyrosine Kinase (BTK) inhibitor acalabrutinib demonstrates potent on-target effects and efficacy in two mouse models of chronic lymphocytic leukemia. *Clin Cancer Res* **23**:2831–2841.

Hibma JE, Zur AA, Castro RA, Wittwer MB, Keizer RJ, Yee SW, Goswami S, Stocker SL, Zhang X, Huang Y, et al. (2016) The effect of famotidine, a MATE1-selective inhibitor, on the pharmacokinetics and pharmacodynamics of metformin. *Clin Pharmacokinet* **55**:711–721.

Hopper M, Gururaja T, Kinoshita T, Dean JP, Hill RJ, and Mongan A (2020) Relative selectivity of covalent inhibitors requires assessment of inactivation kinetics and cellular occupancy: a case study of ibrutinib and acalabrutinib. *J Pharmacol Exp Ther* **372**:331–338.

Jones DR, Gorski JC, Hamman MA, Mayhew BS, Rider S, and Hall SD (1999) Diltiazem inhibition of cytochrome P-450 3A activity is due to metabolite intermediate complex formation. *J Pharmacol Exp Ther* **290**:1116–1125.

Kaptein A, de Bruin G, Emmelot-van Hoek M, van de Kar B, de Jong A, van Lith B, Gulrajani M, Demont D, Covey T, Mittag D, and Barf T (2018) Potency and selectivity of BTK inhibitors in clinical development for B-cell malignancies [poster]. *Blood* **132**(Suppl 1):1871 DOI: https://doi.org/10.1182/blood-2018-99-109973.

Kazmi F, Yerino P, McCoy C, Parkinson A, Buckley DB, and Ogilvie BW (2018) An assessment of the in vitro inhibition of cytochrome P450 enzymes, UDP-glucuronosyltransferases, and transporters by phosphodiester- or phosphorothioate-linked oligonucleotides. *Drug Metab Dispos* **46**:1066–1074.

Kitz R and Wilson IB (1962) Esters of methanesulfonic acid as irreversible inhibitors of acetylcholinesterase. *J Biol Chem* **237**:3245–3249.14033211

Krippendorff BF, Neuhaus R, Lienau P, Reichel A, and Huisinga W (2009) Mechanism-based inhibition: deriving K(I) and k(inact) directly from time-dependent IC(50) values. *J Biomol Screen* **14**:913–923.

Liu Q, Sabnis Y, Zhao Z, Zhang T, Buhrlage SJ, Jones LH, and Gray NS (2013) Developing irreversible inhibitors of the protein kinase cysteinome. *Chem Biol* **20**:146–159.

Lonsdale R and Ward RA (2018) Structure-based design of targeted covalent inhibitors. *Chem Soc Rev* **47**:3816–3830.

Pal Singh S, Dammeijer F, and Hendriks RW (2018) Role of Bruton's tyrosine kinase in B cells and malignancies. *Mol Cancer* **17**:57.

Paris BL, Ogilvie BW, Scheinkoenig JA, Ndikum-Moffor F, Gibson R, and Parkinson A (2009) In vitro inhibition and induction of human liver cytochrome p450 enzymes by milnacipran. *Drug Metab Dispos* **37**:2045–2054.

Podoll T, Pearson PG, Evarts J, Ingallinera T, Bibikova E, Sun H, Gohdes M, Cardinal K, Sanghvi M, and Slatter JG (2019) Bioavailability, biotransformation, and excretion of the covalent Bruton tyrosine kinase inhibitor acalabrutinib in rats, dogs, and humans. *Drug Metab Dispos* **47**:145–154.

Ponader S and Burger JA (2014) Bruton's tyrosine kinase: from X-linked agammaglobulinemia toward targeted therapy for B-cell malignancies. *J Clin Oncol* **32**:1830–1839.

Robertson P, DeCory HH, Madan A, and Parkinson A (2000) In vitro inhibition and induction of human hepatic cytochrome P450 enzymes by modafinil. *Drug Metab Dispos* **28**:664–671.

Scheers E, Leclercq L, de Jong J, Bode N, Bockx M, Laenen A, Cuyckens F, Skee D, Murphy J, Sukbuntherng J, et al. (2015) Absorption, metabolism, and excretion of oral ^{14}C radiolabeled ibrutinib: an open-label, phase I, single-dose study in healthy men. *Drug Metab Dispos* **43**:289–297.

Shadman M, Flinn IW, Levy MY, Porter R, Burke JM, Cultrera JL, Misleh J, Zafar SF, Freeman B, Rao SS, et al. (2021) Phase 2 study of zanubrutinib in BTK inhibitor-intolerant patients (pts) with relapsed/refractory B-cell malignancies (Abstract 1410). *Blood* **138** (Suppl 1):1410.

Singh J, Petter RC, Baillie TA, and Whitty A (2011) The resurgence of covalent drugs. *Nat Rev Drug Discov* **10**:307–317.

Smith DA, Di L, and Kerns EH (2010) The effect of plasma protein binding on in vivo efficacy: misconceptions in drug discovery. *Nat Rev Drug Discov* **9**:929–939.

Smyth LA and Collins I (2009) Measuring and interpreting the selectivity of protein kinase inhibitors. *J Chem Biol* **2**:131–151.

Stopfer P, Marzin K, Narjes H, Gansser D, Shahidi M, Uttereuther-Fischer M, and Ebner T (2012) Afatinib pharmacokinetics and metabolism after oral administration to healthy male volunteers. *Cancer Chemother Pharmacol* **69**:1051–1061.

Strelow JM (2017) A perspective on the kinetics of covalent and irreversible inhibition. *SLAS Discov* **22**:3–20.

Watanabe A, Nakamura K, Okudaira N, Okazaki O, and Sudo K (2007) Risk assessment for drug-drug interaction caused by metabolism-based inhibition of CYP3A using automated in vitro assay systems and its application in the early drug discovery process. *Drug Metab Dispos* **35**:1232–1238.

Zamek-Gliszczynski MJ, Chu X, Cook JA, Custodio JM, Galetin A, Giacomini KM, Lee CA, Paine MF, Ray AS, Ware JA, et al.; International Transporter Consortium (2018) ITC commentary on metformin clinical drug-drug interaction study design that enables an efficacy- and safety-based dose adjustment decision. *Clin Pharmacol Ther* **104**:781–784.

Zhou D, Podoll T, Xu Y, Moorthy G, Vishwanathan K, Ware J, Slatter JG, and Al-Huniti N (2019) Evaluation of the drug-drug interaction potential of acalabrutinib and its active metabolite, ACP-5862, using a physiologically-based pharmacokinetic modeling approach. *CPT Pharmacometrics Syst Pharmacol* **8**:489–499.

Address correspondence to: Dr. Terry Podoll, 4032 SW Myrtle St, Seattle, WA 98136. E-mail: terry.podoll@iv-po.com

Supplemental Information to:

Identification and characterization of ACP-5862, the major circulating active metabolite of acalabrutinib: both are potent and selective covalent BTK inhibitors

Terry Podoll, Paul G. Pearson, Allard Kaptein, Jerry Evarts, Gerjan de Bruin, Maaike Emmelot-van Hoek, Anouk de Jong, Bart van Lith, Hao Sun, Stephen Byard, Adrian Fretland, Niels Hoogenboom, Tjeerd Barf, and J. Greg Slatter

Journal of Pharmacology and Experimental Therapeutics

Manuscript number: JPET-AR-2022-001116R1

Supplemental Methods

ACP-5862 Semipreparative High-performance Liquid Chromatography (HPLC) Purification (M25). The combined fractions for metabolite M25 were evaporated to dryness under a stream of nitrogen and reconstituted in 300 µl of 9:1 (v:v) water:methanol (MeOH). The reconstituted M25 sample was further isolated on an analytical scale by injection onto a Hewlett Packard 1100 series HPLC system and separation on an Xterra column (4.6 × 150 mm, 5 µm, Waters). Mobile phase components 10 mM ammonium bicarbonate (pH 9; A), and acetonitrile (B) were pumped at 1.0 ml/minute beginning at 10% B, held for 10 minutes, then followed by a linear gradient to 25% B at 40 minutes, held for 5 minutes, increased to 90% B at 50 minutes, held until 55 minutes to wash the column, and re-equilibrated to initial conditions for 9 minutes. Eluent fractions were collected at 30-second intervals into vials. The fractions corresponding to M25 according to radioactivity data were combined, and an aliquot was taken to confirm its purity by liquid chromatography (LC)-high resolution mass spectrometry (MS). The combined fractions for metabolite M25 were evaporated to dryness under a vacuum.

ACP-5862 Semipreparative HPLC Purification. To isolate metabolites M25 and M27, the reconstituted sample was repeatedly injected (n = 9) onto a Hewlett Packard 1100 series HPLC system and separated on a semi-preparative column (YMC-Pack ODS-AQ, 10 × 250 mm, 5 µm, YMC Co.). Mobile phase components 0.1% formic acid (A) and acetonitrile (B) were pumped at 4.0 ml/minute beginning at 10% B followed by a linear gradient to 25% B at 40 minutes, an increase to 90% B at 42 minutes, held until 45 minutes to wash the column, and re-equilibrated to initial conditions for 15 minutes. Eluent fractions were collected at 30-second intervals into vials. Aliquots of all fractions potentially associated with metabolite M25 or M27 were analyzed by LSC. Based on the radioactivity data, multiple fractions corresponding to each of the metabolites were combined, as necessary. The combined fractions for metabolite M27 were concentrated under a stream of nitrogen, and an aliquot was taken to confirm the purity by LC-MS. Chromatograms of the purified M27 extract, fresh microsomal incubation extract, and fresh microsomal incubation extract that was spiked with purified M27 were compared. The sample was then evaporated to dryness.

ACP-5862 Nuclear Magnetic Resonance (NMR) Sample Preparation. The samples of metabolites M25 and M27 were each dissolved in 0.15 ml deuterated methanol (CD_3OD, Cambridge Isotope Laboratories, Andover, MA) and were subsequently transferred to high-precision 2.5-mm-OD capillary NMR tubes. Analyses were initiated within 60 minutes of dissolving the material in deuterated solvent, following optimization and stabilization of the magnet. The approximate sample masses employed for the study were 25 μg and 100 μg for metabolites M25 and M27, respectively.

ACP-5862 NMR Spectroscopy. All NMR experiments were performed using a Bruker DRX500 spectrometer equipped with an 11.7 Tesla magnet. Spectra were acquired using a 2.5-mm TXI ^{1}H - ^{13}C/^{15}N z-gradient inverse geometry probe. Sample temperatures were controlled throughout the analyses at 293K, with appropriate time allowed for establishment of thermal equilibrium.

^{1}H NMR-spectra were acquired using a direct pulse-acquire sequence, a spectral width of 7.0 kHz, and a total acquisition time of 4.7 s. The relaxation delay for the 1D experiment was 1 s, while all 2D experiments described below employed a 2-s relaxation delay. Chemical shifts were referenced using the residual proton signal of CD_3OD relative to tetramethylsilane ($\delta = 0.00$). Exponential multiplication convolution factors of 0.1 Hz and 0.3 Hz were applied to the free induction decays prior to Fourier transformation for metabolites M25 and M27, respectively. For metabolite M27, presaturation at the frequency of water/CD_3OH was applied throughout the relaxation period. ^1H homonuclear shift correlation (COSY) and ^1H – ^1H total correlation (TOCSY) spectra were acquired using a spectral width of 5.0 kHz in the F1 and F2 dimensions and an acquisition time of 409.8 ms. The COSY spectra were acquired with 64 transients per increment (8 dummy transients) and 512 increments with linear prediction to 1024. The TOCSY spectra were acquired using Malcom Levitt's decoupling cycle (MLEV) spin lock for mixing, and there were 136 (M25) or 128 (M27) transients per increment (16 dummy transients). The spectrum was phase sensitive, using echo/anti-echo gradient selection. Phase-sensitive gradient-selected echo/anti-echo, ^1H – ^{13}C one-bond single-quantum correlation (HSQC) experiments, using double inept transfer with sensitivity improvement, were acquired using a spectral width of 5.0 kHz in the F2 dimension, an acquisition time of 205.0 ms, and 200 (M25) or 64 (M27) transients per increment (16 dummy transients). A gradient-selected echo/anti-echo, ^1H – ^{13}C 2/3-bond multiple-quantum correlation (HMBC) experiment was acquired for metabolite M27 using a spectral width of 5.0 kHz in the F2 dimension, an acquisition time of 409.8 ms, and 256 transients per increment (16 dummy transients).

Supplemental Results

Structure Elucidation of M25 and M27 by NMR. The ^1H NMR spectra of the pure biosynthetic metabolites M25 and M27 were compared with acalabrutinib. Aromatic proton signals of acalabrutinib were all present in the metabolites. The aliphatic region defined sites of biotransformation in the pyrrolidine moiety.

The ^1H NMR peak assignments for metabolite M25 are shown in Table S4, and the spectrum is shown in Supplemental Fig. S2. A triplet at 6.08 ppm was consistent with an olefin coupled to a methylene. Coupling was investigated using a double-quantum filtered ^1H – ^1H homonuclear shift correlation experiment (COSY; Supplemental Fig. S3), and a total correlated ^1H – ^1H homonuclear shift experiment (TOCSY; Supplemental Fig. S4) to support the final assignments (Table S4). Multiple signals in the spectra were associated with chemically equivalent nuclei. The sum of the integrals of the paired signals totals a value which is integrally related to that of the signal at 6.08 ppm, exemplifying that this is the split of the chemically equivalent methyl protons. Like the acalabrutinib NMR spectrum, the methyl signals of M25 exist as two singlets, with a relative intensity ratio that matches those of the other paired signals. Signals at 1.47 ppm (s) and 2.10 ppm (s) were assigned to the methyl protons of the metabolite, based in part on their total integral value. The splitting of the aliphatic signals was ascribed to a conformational exchange around the amide bond in the pyrrolidine ring, which is slow on the NMR timescale. A similar effect was observed for acalabrutinib (Barf et al., 2017), showing that the desaturated pyrrolidine ring (a dihydropyrrole) remains intact in M25. The position of the double bond is assigned based on chemical shifts of H_c and $H_{c'}$, in conjunction with the multiplicity of the signal associated with H_d. Due to the relatively low quantity of M25 available, not all signals were observed in a ^1H – ^{13}C 1-bond heteronuclear correlation spectrum (Supplemental Fig. S5); however, the carbon chemical shifts associated with the 2 conformations are observed, in particular for protons labelled H_b/H_b' and H_c/$H_{c'}$. The assigned double bond sits in conjugation with the heteroaryl moiety of acalabrutinib and is a logical dehydration product of the carbinolamide precursor of M27.

The ^1H NMR peak assignments of metabolite M27 are summarized in Table S5, and the aliphatic region of the spectrum is shown in Supplemental Fig. S6 and Fig. S7. The aliphatic region spectrum comprised 4 resonances, all having clear and discernible multiplicities, with 1 signal present for each chemically equivalent nucleus. The peaks show that the pyrrolidine ring of acalabrutinib has opened, since geminally coupled pairs of protons may otherwise be expected. Additionally, there was no evidence of inversion of the amide bond, indicating a ring-opened structure. To confirm chemical shift information, TOCSY (Supplemental Fig. S8) and COSY (Supplemental Fig. S9) data were acquired. Only three chemically different proton types are present in the aliphatic spin system of interest (H_b, H_c, and H_d in Table 2 of main article), in addition to the isolated methyl moiety. All three-bond couplings in the COSY spectrum are unequivocally consistent with an open chain of three methylene units. A ^1H – ^{13}C heteronuclear single-quantum coherence experiment (Supplemental Fig. S10) provided ^{13}C chemical shifts of the three methylene groups and indirect confirmation of two carbonyl moieties (summarized in Table S6).

Reference

Barf T, Covey T, Izumi R, van de Kar B, Gulrajani M, van Lith B, van Hoek M, de Zwart E, Mittag D, Demont D, Verkaik S, Krantz F, Pearson PG, Ulrich R and Kaptein A (2017) Acalabrutinib (ACP-196): A covalent Bruton tyrosine kinase inhibitor with a differentiated selectivity and in vivo potency profile. *J Pharmacol Exp Ther* **363**:240-252.

TABLE S1

Relative selectivity of acalabrutinib, ACP-5862, ibrutinib, and zanubrutinib versus respective BTK potency on other kinases with a cysteine in the same position as Cys481 in BTK

	Selectivity versus BTK			
Kinase	**Acalabrutinib**[d]	**ACP-5862**	**Ibrutinib**	**Zanubrutinib**
BTK[a] IC$_{50}$ (nM)	5.1 ± 1.0	5.0 ± 1.0	1.5 ± 0.2	0.5 ± 0.0
TEC[b]	25	69	7	88
ITK[a]	>200	>200	3	100
BMX[c]	9	3	1	3
TXK[c]	72	113	1	4
EGFR[c]	>200	>200	4	42
ERBB2[c]	~200	110	4	176
ERBB4[c]	3	69	2	14
BLK[c]	>200	>200	<1	5
JAK3[c]	>200	>200	21	>2000

Values were determined from the individual IC$_{50}$/BTK IC$_{50}$ ratios from [a]IMAP assay, [b]LanthaScreen assay, [c]at Thermo Fisher using the Z´-LYTE assay, Table 1) for the respective BTK inhibitors. [d]Results from previous studies (Barf et al., 2017; Kaptein et al., 2018). Ibrutinib and zanubrutinib data included as points of reference to marketed, selective BTK inhibitors.

Note: BTK IC$_{50}$ mean ± SD from at least 3 independent assay runs.

BLK, B-lymphocyte kinase; BMX, BMX non-receptor tyrosine kinase; BTK, Bruton tyrosine kinase; EGFR, epidermal growth factor receptor; ERBB, erythroblastosis oncogene B; IC$_{50}$, inhibitory concentration 50%; ITK, interleukin-2-inducible T-cell kinase; JAK3, Janus-associated kinase 3; TEC, tec protein tyrosine kinase; TXK, TXK tyrosine kinase/protein tyrosine kinase.

TABLE S2

Inhibition of P450 and UGT isoforms by acalabrutinib and ACP-5862 in HLMs

	Acalabrutinib			ACP-5862		
P450 or UGT enzyme	**IC_{50} (μM) No preincubation**	**IC_{50} (μM) Preincubation minus NADPH**	**IC_{50} (μM) Preincubation plus NADPH**	**IC_{50} (μM) No preincubation**	**IC_{50} (μM) Preincubation minus NADPH**	**IC_{50} (μM) Preincubation plus NADPH**
CYP1A2	No inhibition	No inhibition	No inhibition	No inhibition	No inhibition	No inhibition
CYP2B6	>100	>100	>100	No inhibition	No inhibition	>20
CYP2C8	37	45	18	>20	>20	3.9
CYP2C9	28	29	14	6.7	10	6.5
CYP2C19	>100	>100	>100	17	15	15
CYP2D6	>100	>100	>100	>20	>20	>20
CYP3A4/5[a]	57	58	13	No inhibition	No inhibition	>20
CYP3A4/5[b]	69	76	16	No inhibition	No inhibition	>20
UGT1A1	No inhibition	N/A	N/A	>3	N/A	N/A
UGT2B7	No inhibition	N/A	N/A	No inhibition	N/A	N/A

Note: Average data (i.e., percent of control activity) obtained from duplicate samples for each test article concentration were used to calculate IC_{50} values.

[a]Testosterone as substrate; [b]midazolam as substrate.

HLMs, human liver microsomes; IC_{50}, inhibitory concentration 50%; N/A, not applicable; NADPH, nicotinamide adenine dinucleotide phosphate.

TABLE S3

Uptake transporter inhibition by acalabrutinib and ACP-5862

		Acalabrutinib		**ACP-5862**	
		I_{max} = 1.45 µM; $I_{max,u}$ = 0.036 µM		I_{max} = 0.84 µM; $I_{max,u}$ = 0.012 µM	
Transporter	**Substrate**	**IC_{50} (µM)**	**Static model interpretation Potential for clinical (Y/N)**	**IC_{50} (µM)**	**Static model interpretation Potential for clinical (Y/N)**
OATP1B1	[^{3}H]Estradiol 17-β-glucuronide	None	No	10.1	No
OATP1B3	[^{3}H]Estradiol 17-β-glucuronide	None	No	>20	No
OAT1	[^{3}H]p-Aminohippuric acid	None	No	12.1	No
OAT3	[^{3}H]Estrone 3-sulfate	>20	No	None	No
OCT2	[^{14}C]Metformin	Approx. 20	No	>20	No
MATE1	[^{14}C]Metformin	>3	No	0.2	Yes
MATE2K	[^{14}C]Metformin	None	No	>3	No

None = No inhibition observed; For interpretation IC_{50} = K_i.

IC_{50}, inhibitory concentration 50%; I_{max}, maximal inhibition; $I_{max,u}$, maximal unbound plasma concentration; K_i, unbound inhibition constant; MATE1, multidrug and toxin extrusion protein 1; MATE2K, multidrug and toxin extrusion protein 2K; OAT1, organic anion transporter 1; OAT 3, organic anion transporter 3; OATP1B1, organic anion transporting polypeptides family member 1B1; OATP1B3, organic anion transporting polypeptides family member 1B3; OCT2, organic cation transporter 2.

TABLE S4

Selected ^{1}H NMR assignments for acalabrutinib metabolite M25 to confirm the site of pyrrolidine ring modification

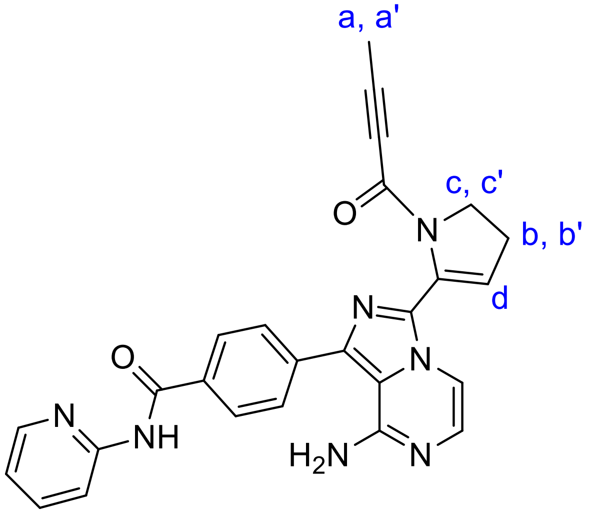

δ_H/ppm	Integral[a]	Multiplicity	COSY (TOCSY)	Assignment
1.47	2.0	s	-	a
2.10	1.0	s	-	a’
2.92	2.0	Triplet of doublets	c, d (c, d)	b
2.95		Triplet of doublets	c’, d (c’, d)	b’
4.21	1.4	Triplet	b (b, d)	c
4.42	0.7	Triplet	b’ (b’, d)	c’
6.08	1.0	Triplet	b, b’ (b, b’, c, c’)	d

[a] The integral values have been quoted to 1 decimal place to indicate the proportion of conformational forms.

COSY, ^{1}H homonuclear shift correlation; NMR, nuclear magnetic resonance; ppm, parts per million; TOCSY, ^{1}H – ^{1}H total correlation.

TABLE S5

Selected ^{1}H NMR assignments for acalabrutinib metabolite M27 to confirm the site of metabolism

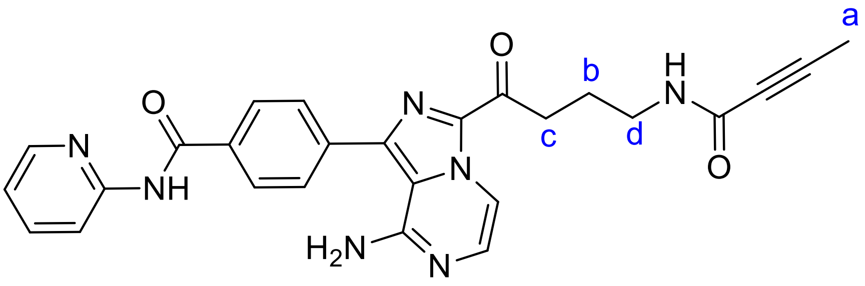

δ$_H$/ppm	Integral	Multiplicity	COSY (TOCSY)	Assignment
1.90	3	s	-	a
1.99	2	Quintet	c, d (c, d)	b
3.26	2	Triplet	b (b, d)	c
3.32	2[a]	Triplet	b (b, c)	d

[a] The signal at 3.32 ppm overlaps with that of CD$_2$HOD, and the integral was determined as an *inter alia* value in conjunction with the ^{1}H – ^{13}C correlation data.

COSY, ^{1}H homonuclear shift correlation; NMR, nuclear magnetic resonance; ppm, parts per million; TOCSY, ^{1}H – ^{1}H total correlation.

TABLE S6

Selected ^{13}C NMR assignments for acalabrutinib metabolite M27 to confirm the site of metabolism

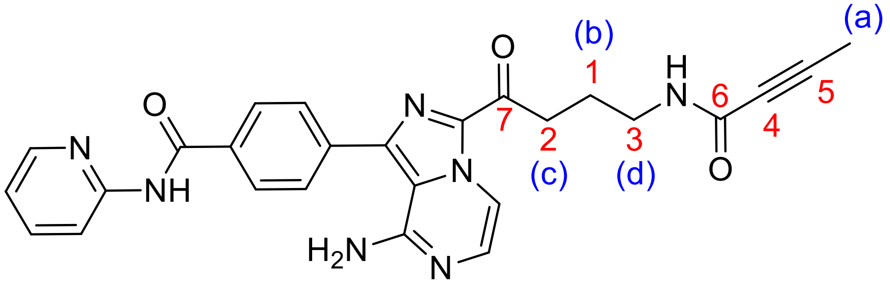

δ_C/ppm	^{1}H – ^{13}C 1-bond connectivity	^{1}H – ^{13}C 2/3-bond connectivity	Assignment
23.4	b	c, d	1
36.0	c	d	2
38.6	d	b, c	3
73.5	-	a	4[a]
83.4	-	a	5[a]
154.5	-	a, d	6
191.4	-	b, c	7

[a] Assignments for carbon nuclei labelled C_4 and C_5 are regarded as interchangeable, as they were assigned on the basis of acalabrutinib. They are included to demonstrate the presence of the alkyne moiety.

NMR, nuclear magnetic resonance; ppm, parts per million.

Figure S1 Extracted ion chromatogram (m/z 482) from analysis of a mixed standard solution containing pyrrolidine-hydroxylated standards representing potential acalabrutinib-related metabolites with structures shown below.

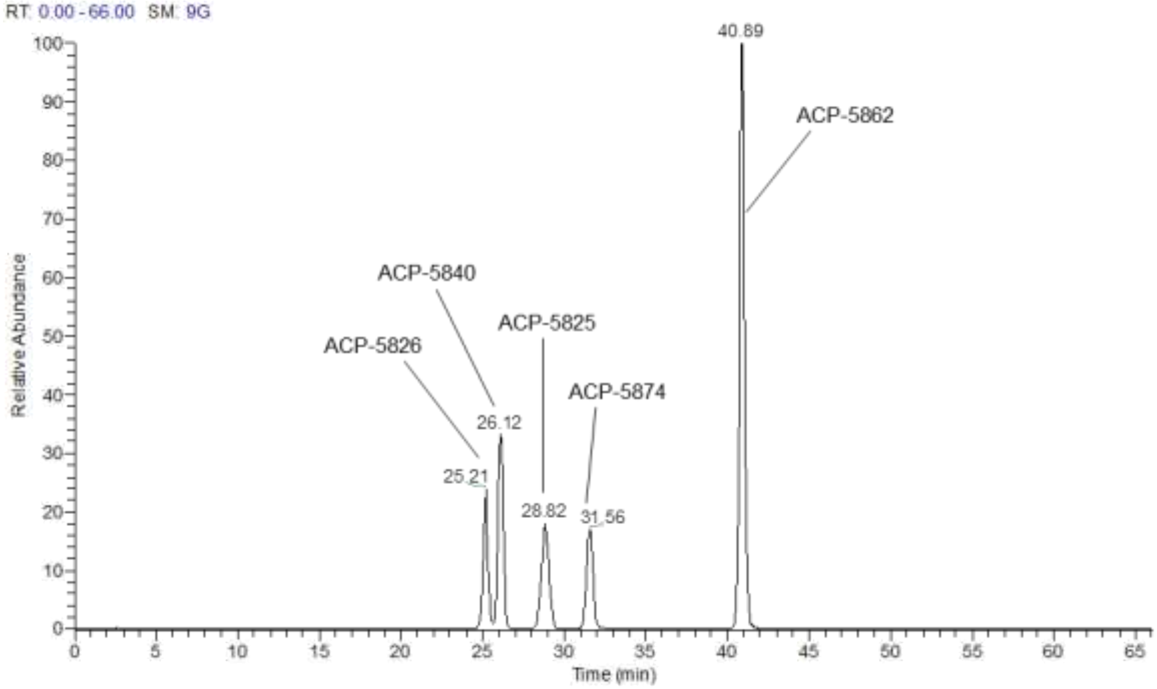

ACP-5826	ACP-5840	ACP-5825	ACP-5874	ACP-5862
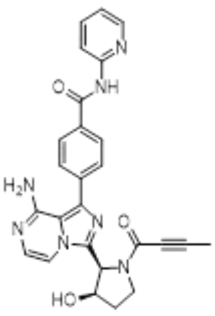	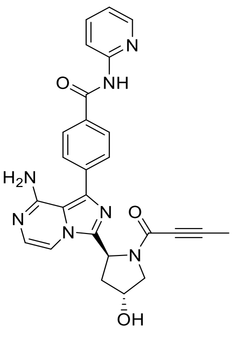	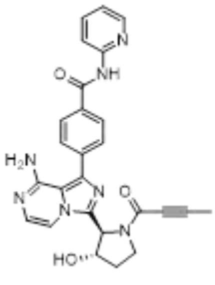	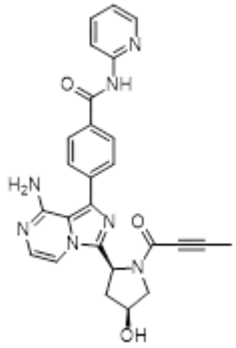	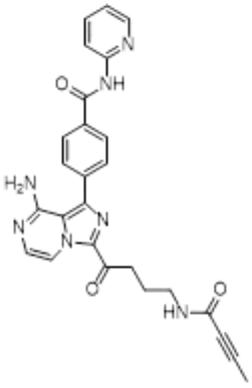

Figure S2. Expanded regions of the ^{1}H nuclear magnetic resonance spectrum of acalabrutinib metabolite M25 dissolved in CD_3OD, acquired at 293K.

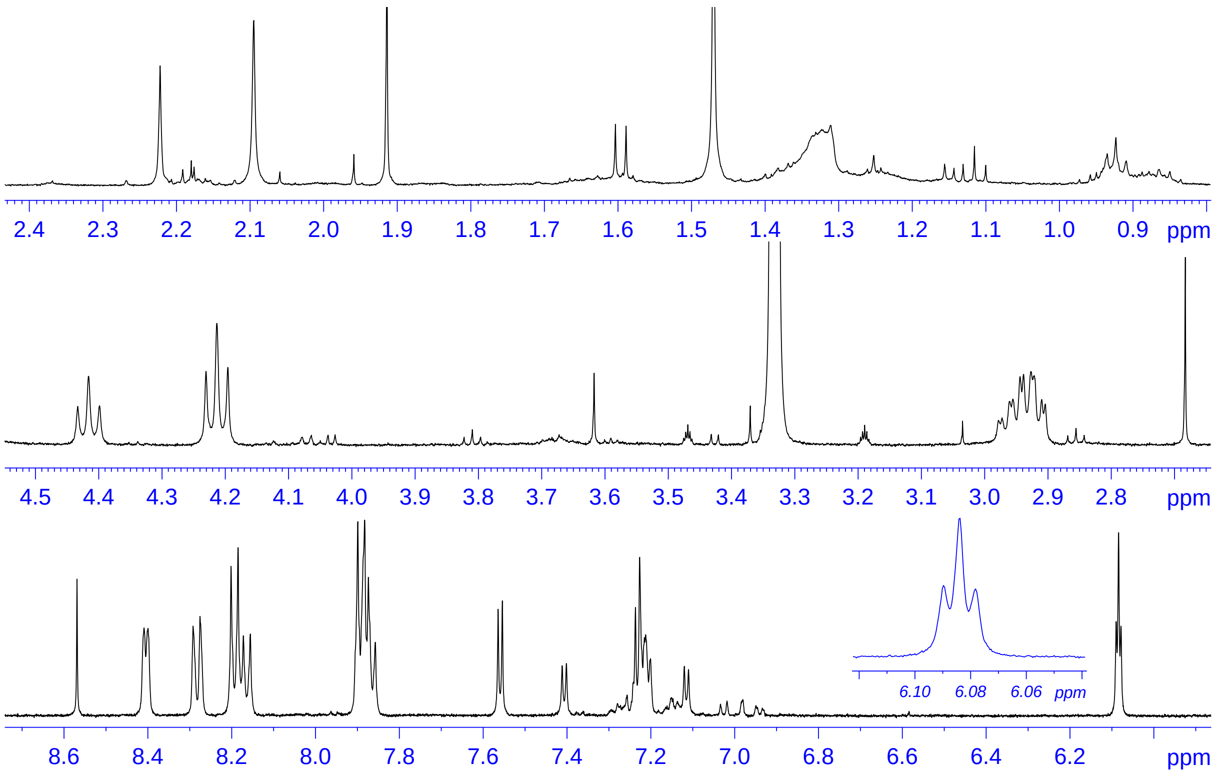

Figure S3. An expanded aliphatic region of the ^1H – ^1H gradient selected, double quantum filtered, homonuclear shift correlation nuclear magnetic resonance spectrum of acalabrutinib metabolite M25 dissolved in CD_3OD, acquired at 293K.

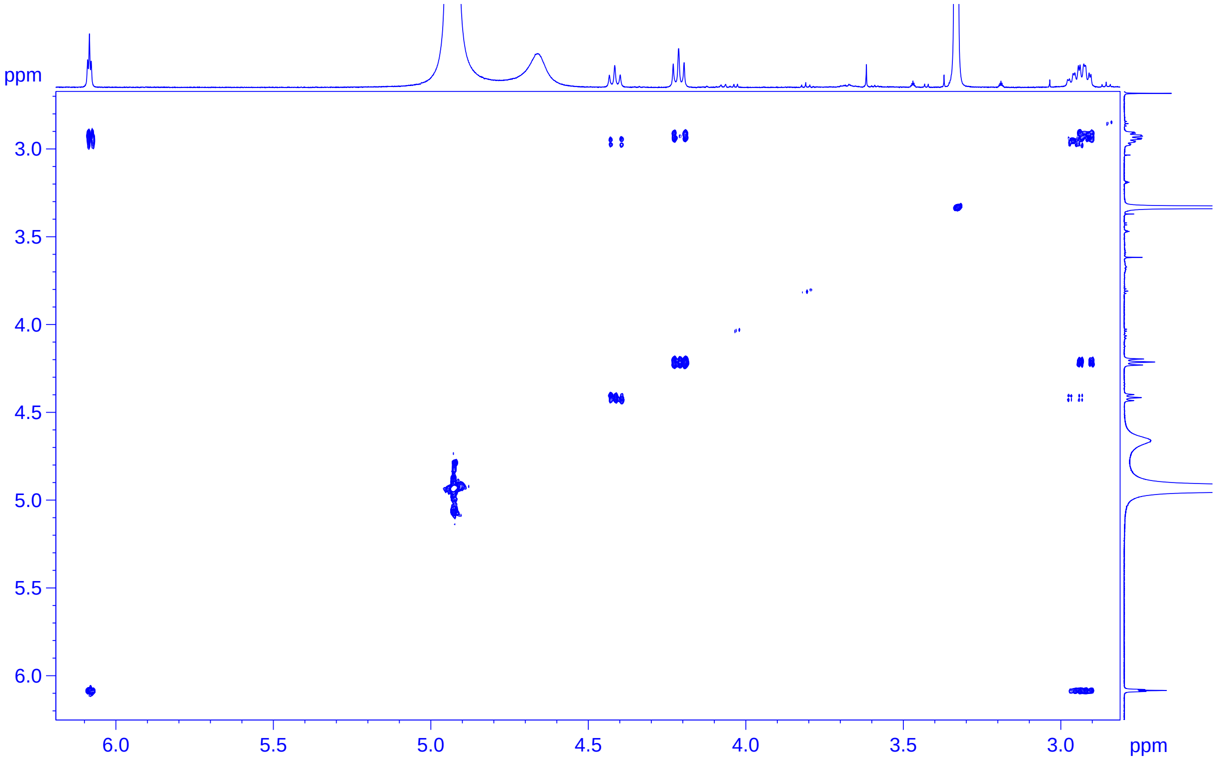

Figure S4. The expanded aliphatic region of the ^{1}H – ^{1}H gradient selected total correlation nuclear magnetic resonance spectrum of acalabrutinib metabolite M25 dissolved in CD_3OD, acquired at 293K.

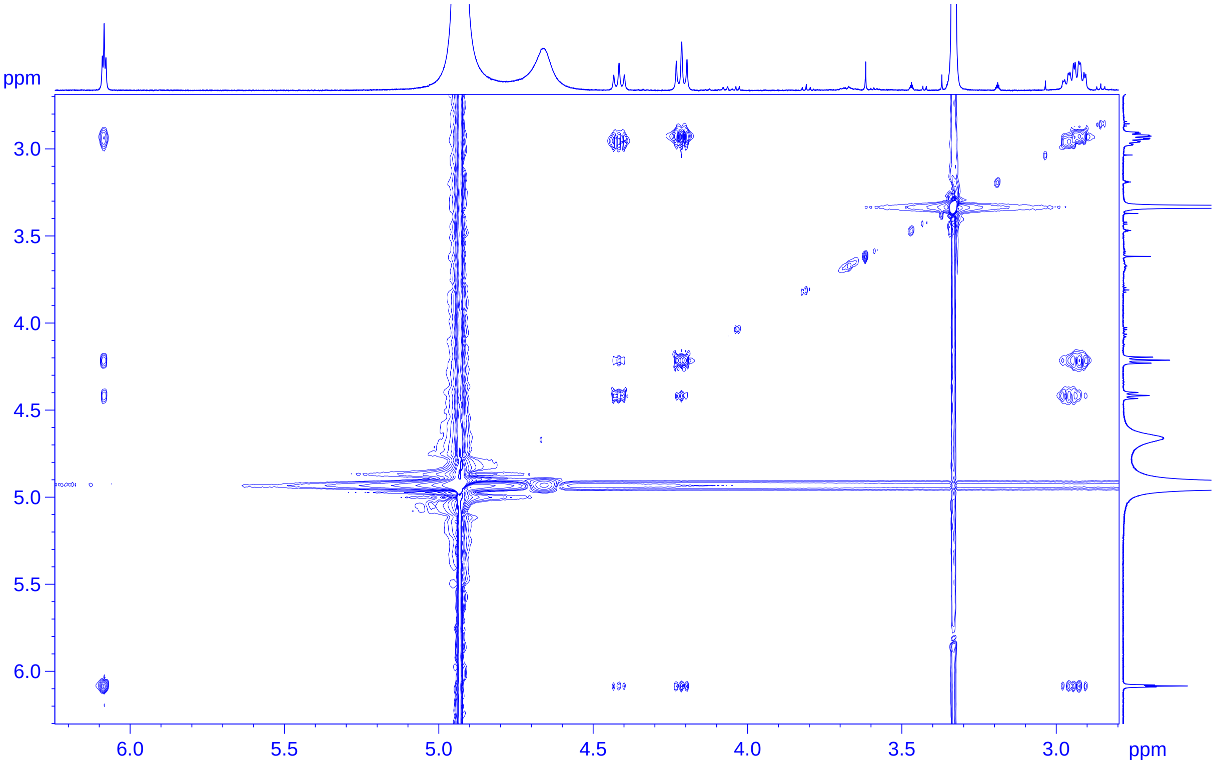

Figure S5. The ^{1}H – ^{13}C gradient selected heteronuclear single quantum (1-bond) correlation nuclear magnetic resonance spectrum of acalabrutinib metabolite M25 dissolved in CD_3OD, acquired at 293K.

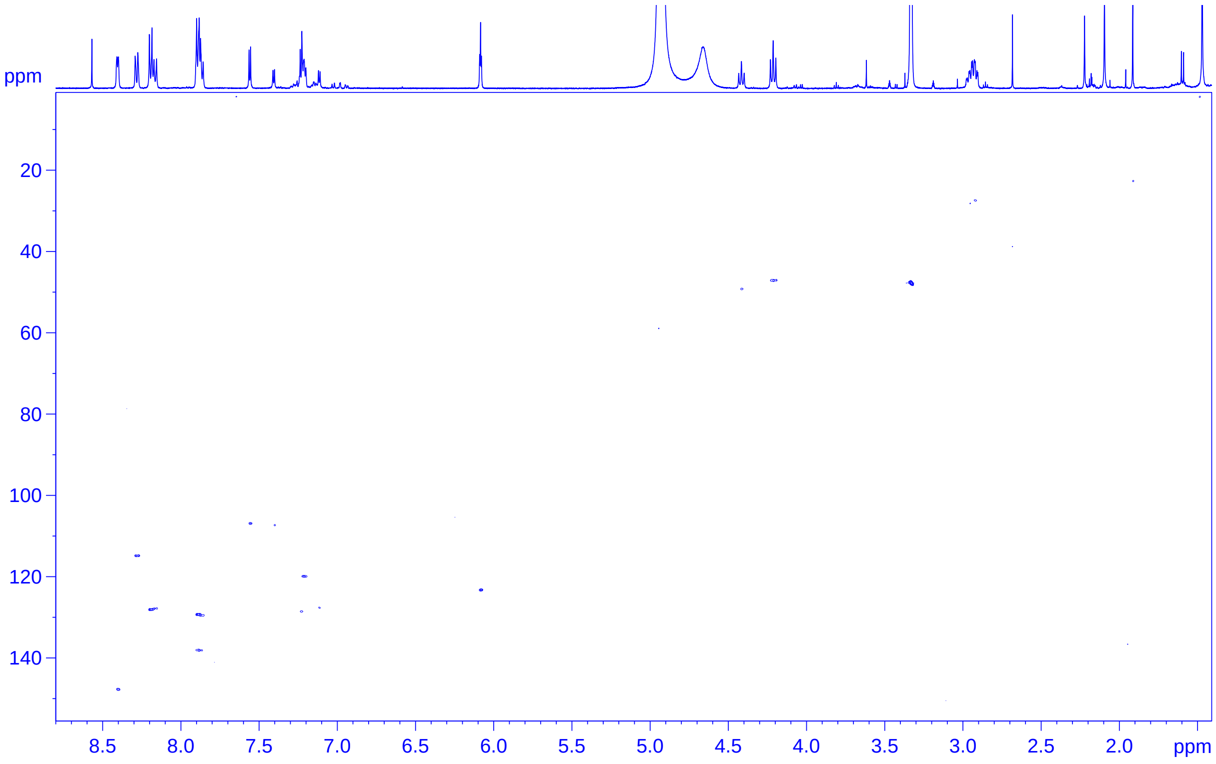

Figure S6. An expanded low-frequency aliphatic region of the ^{1}H nuclear magnetic resonance spectrum of acalabrutinib metabolite M27 dissolved in CD_3OD, acquired at 293K.

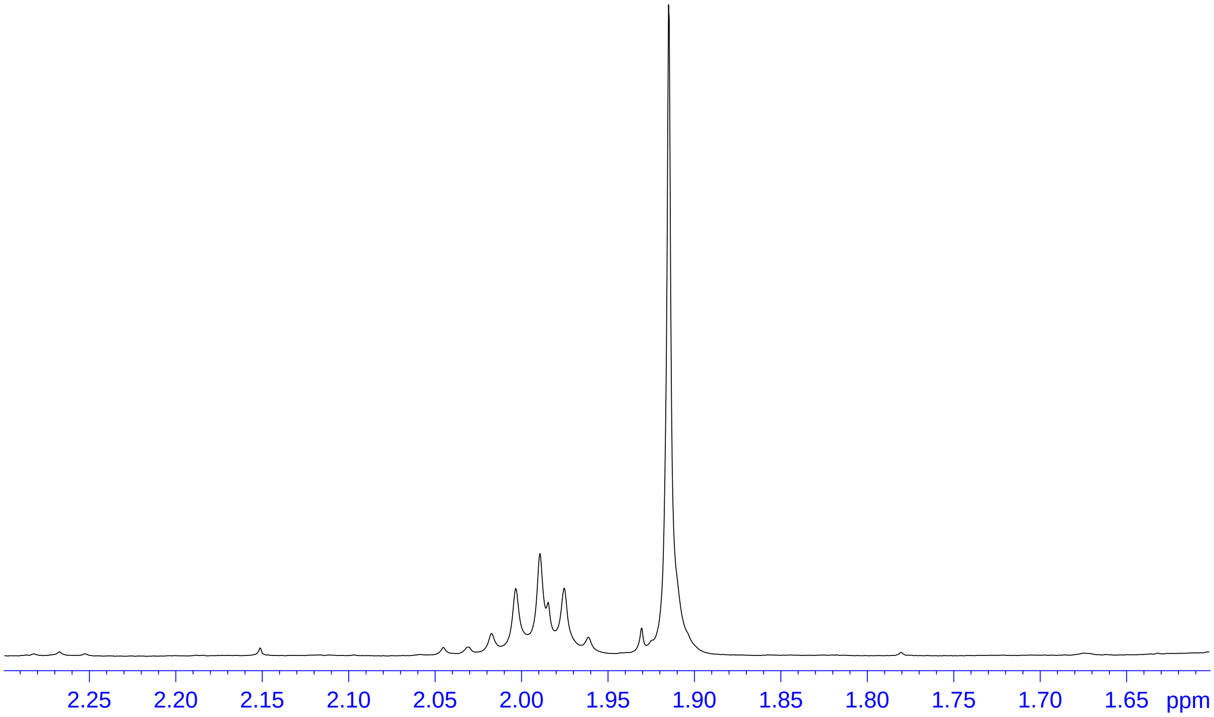

Figure S7. An expanded high-frequency aliphatic region of the ^{1}H nuclear magnetic resonance spectrum of acalabrutinib metabolite M27 dissolved in CD_3OD, acquired at 293K.

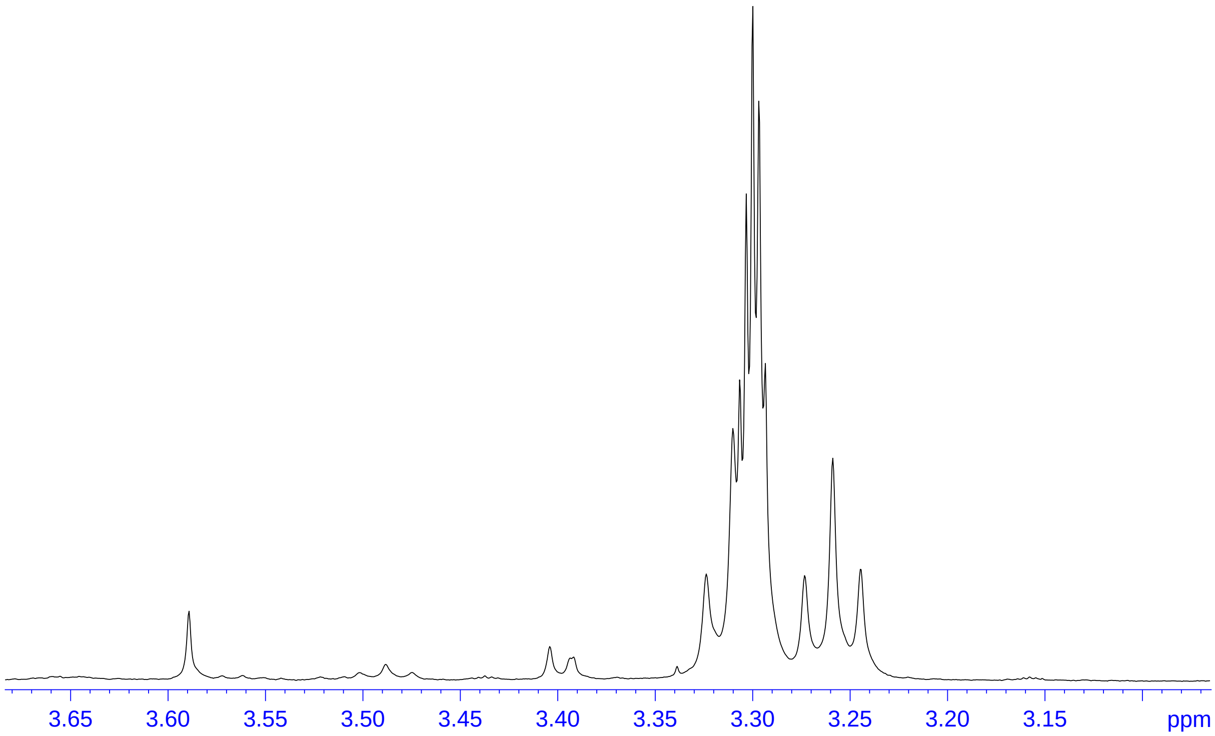

Figure S8. An expanded aliphatic region of the ^1H – ^1H gradient selected total correlation nuclear magnetic resonance spectrum of acalabrutinib metabolite M27 dissolved in CD_3OD, acquired at 293K.

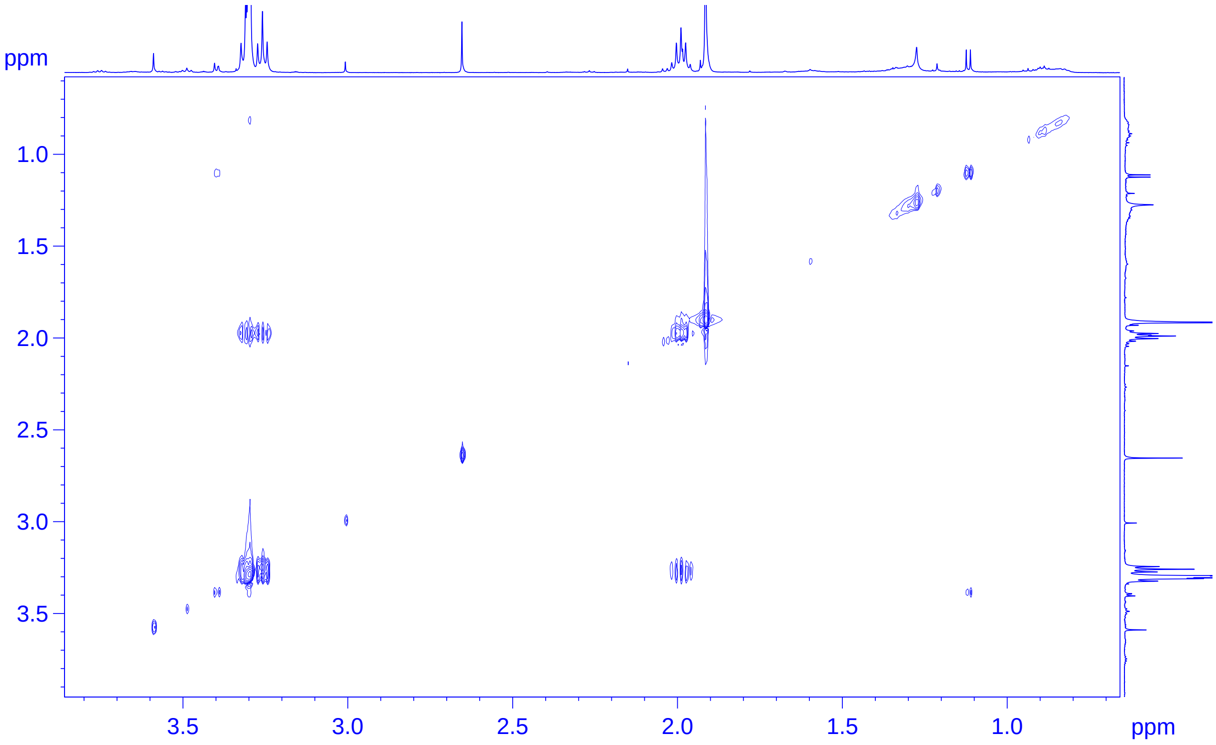

Figure S9. An expanded region of the ^1H – ^1H gradient selected, double quantum filtered, homonuclear shift correlation nuclear magnetic resonance spectrum of acalabrutinib metabolite M27 dissolved in CD_3OD, acquired at 293K.

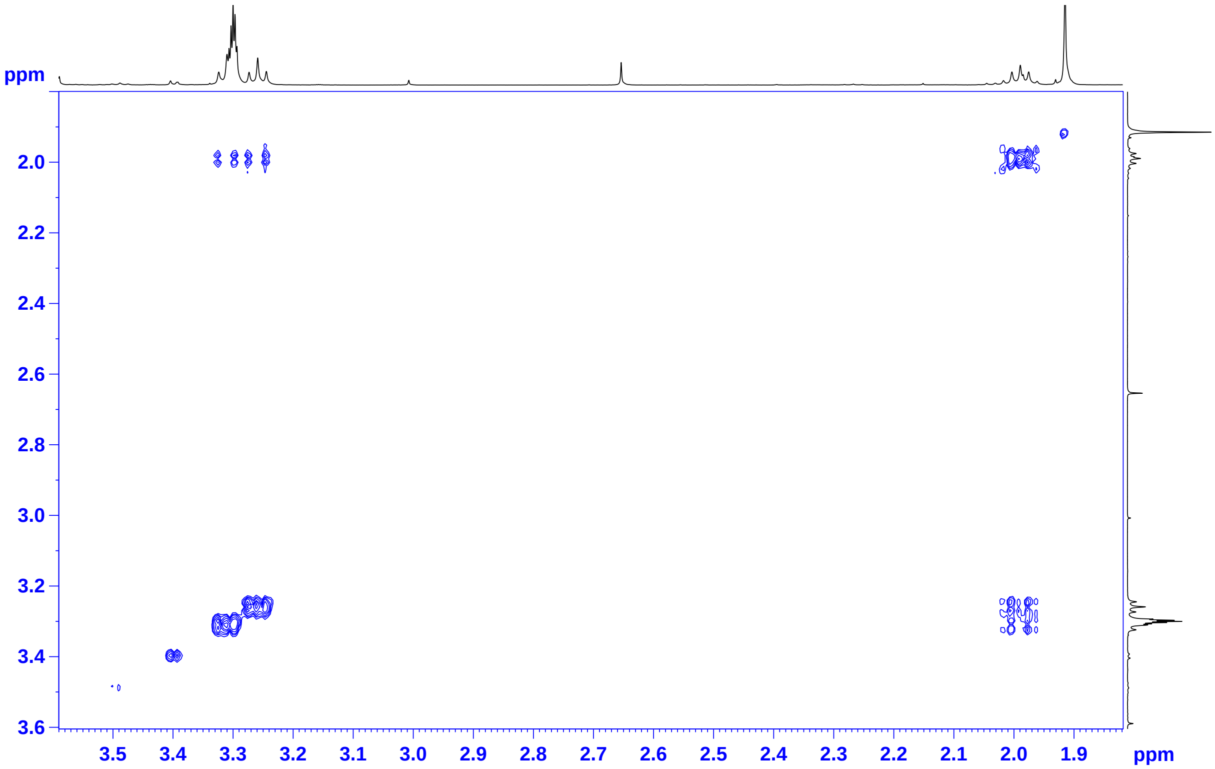

Figure S10. **An expanded region of the ^{1}H – ^{13}C gradient selected heteronuclear single quantum (1-bond) correlation nuclear magnetic resonance spectrum of acalabrutinib metabolite M27 dissolved in CD_3OD, acquired at 293K.**

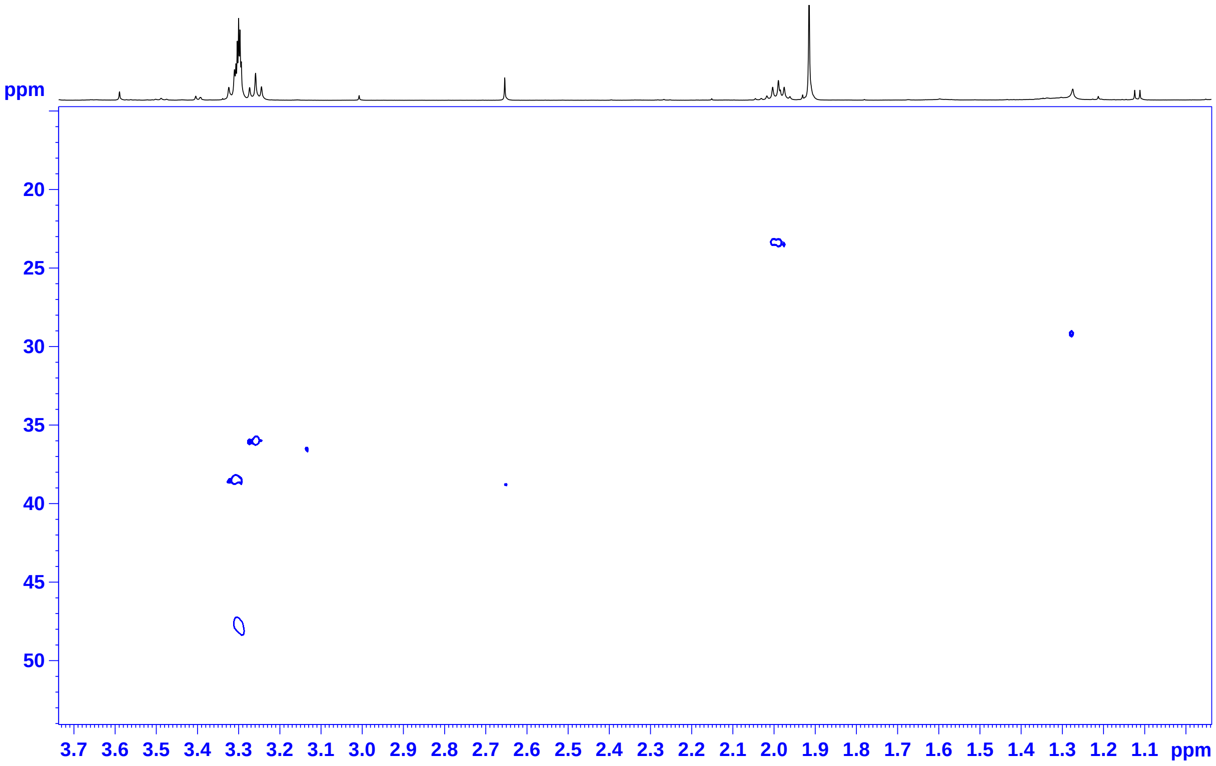
ppm
20
25
30
35
40
45
50
3.7 3.6 3.5 3.4 3.3 3.2 3.1 3.0 2.9 2.8 2.7 2.6 2.5 2.4 2.3 2.2 2.1 2.0 1.9 1.8 1.7 1.6 1.5 1.4 1.3 1.2 1.1 ppm